High-Temperature Materials

SCIEPublish

Article

# Study on the Redox Behavior and Reactive Oxygen Site of Reducible $A_2B_2O_7$ Composite Oxides

**Xiaomei Yu [1,†], Junwei Xu [1,2,*,†], Wenkai Ruan [1], Yong Fu [1], Lei Mao [1] and Xiang Wang [1,*]**

[1] Key Laboratory of Jiangxi Province for Environment and Energy Catalysis, School of Chemistry and Chemical Engineering, Nanchang University, Nanchang 330031, China; XiaomeiYu@email.ncu.edu.cn (X.Y.); wenkaiRuan@email.ncu.edu.cn (W.R.); YongFu@email.ncu.edu.cn (Y.F.); leimao@email.ncu.edu.cn (L.M.)

[2] Jiangxi Academy of Sciences, Nanchang 330096, China

* Corresponding author. E-mail: xujunwei@email.ncu.edu.cn (J.X.); xwang23@ncu.edu.cn (X.W.)

† These authors contributed equally to this work.

Received: 20 July 2026; Revised: 13 August 2026; Accepted: 8 October 2026; Available online: 26 October 2026

**ABSTRACT:** In this study, a series of reducible $A_2B_2O_7$ composite oxides was synthesized using a simple citric acid sol-gel method. Different characterization techniques were employed to reveal the essential factors affecting the redox properties and surface chemically adsorbed oxygen species of these compounds. The results indicate that the redox properties of ionic oxides of the A-site and B-site influence the redox behavior of the corresponding $A_2B_2O_7$ compounds, while the rigidity and looseness of the sub-crystal phase structure, as well as the lattice disorder degree, of these compounds affect the amount of surface chemisorbed oxygen. The type of sub-crystalline structure and lattice disorder are essential factors influencing the amount of chemisorbed oxygen species, with the order being disordered solid solution/disordered defect fluorite > pyrochlore > layered perovskite. Furthermore, it was found that the lattice disorder degree of $Pr_2Zr_2O_7$ and $Tb_2Zr_2O_7$ increases due to the complete reduction of $Pr^{4+}$ or $Tb^{4+}$ to $Pr^{3+}$ and $Tb^{3+}$ in a high-temperature reducing atmosphere (>600 °C). Similarly, disordered defect fluorite structures, such as $Pr_2Ce_2O_7$ and $Tb_2Ce_2O_7$, transform into rare-earth C-type crystalline structures in the same reducing atmosphere.

**Keywords:** Reducible $A_2B_2O_7$ composite oxide; Sub-crystalline phase; Redox property; Reactive oxygen site

## 1. Introduction

$A_2B_2O_7$ composite oxides are extensively utilized in oxygen ion conduction and heterogeneous thermal catalytic reactions due to their high thermal stability, structural openness, tunability, and excellent oxygen ion conductivity [1,2]. They have been particularly studied in methane reforming, catalytic combustion of soot particles, catalytic methane combustion, and oxidative coupling of methane reactions [2]. For these reactions, the active oxygen on the surface and redox properties of $A_2B_2O_7$ compounds are crucial. For instance, in the dry reforming of methane, surface active oxygen is beneficial for eliminating carbon

© 2026 The authors. This is an open access article under the Creative Commons Attribution 4.0 International License (https://creativecommons.org/licenses/by/4.0/).

deposition [3]. It can also promote the catalytic combustion of soot particles [4], facilitate the activation of 0methane in methane activation reactions, and affect the types of products [2].

When certain $A_2B_2O_7$ compounds are utilized as carriers for loading metals as catalysts—such as nickel-based or noble metal-based catalysts for methane dry reforming—their precursors consist of the corresponding metal oxides that are loaded onto $A_2B_2O_7$ [3]. These metal oxides are formed through hydrogen reduction at specific temperatures. However, the majority of studies rely on ex situ testing, which poses a risk of oxidation by atmospheric oxygen after the pretreatment and removal of samples. This limitation prevents a true representation of their actual structure during the catalytic process. In addition, studies have demonstrated that the presence of redox sites on metal oxide surfaces is advantageous for low-temperature deep oxidation of methane and ODHE reactions [2].

Wang et al. systematically compared the active sites and structure–activity relationships of perovskites ($ABO_3$) and pyrochlores ($A_2B_2O_7$) in the OCM reaction, and pointed out that the sub-crystalline phase structure, lattice disorder degree, B–O bond covalency, oxygen vacancy concentration, and surface basicity jointly determine the OCM catalytic performance [5]. $A_2B_2O_7$ exists in four sub-crystalline phases: layered perovskite, pyrochlore, disordered defective fluorite, and rare-earth C-type, and their lattice disorder degree and oxygen vacancy concentration follow the order disordered defect fluorite > rare-earth C-type > disordered pyrochlore > ordered pyrochlore. The weaker the B–O bond covalency, the lower the oxygen vacancy formation energy, and the easier the lattice oxygen desorption, which is more favorable for $C_2$ selectivity; the synergy between oxygen vacancies and surface basic sites can stabilize reactive oxygen species such as $O_2^-$ and $O_2^{2-}$, enhancing low-temperature OCM performance [5]. For OCM reactions, it is widely accepted that chemisorbed oxygen species enhance $C_2$ selectivity, whereas surface-active lattice oxygen species facilitate the deep oxidation of methane [6]. Furthermore, we also found that compounds such as $Pr_2Ce_2O_7$ exhibit a fluorite crystal phase structure at room temperature, but undergo a transformation into a rare earth C-type crystal phase after being reduced at high temperatures in a $H_2$-Ar mixed gas atmosphere [7]. The subtle changes in the sub-crystal phase structure of these reducible $A_2B_2O_7$ compounds need to be observed in a reducing gas atmosphere, which is helpful for a deeper understanding of their structural changes. Therefore, it is essential to elucidate the redox properties of reducible $A_2B_2O_7$ compounds and the factors that influence them. The study further discussed that surface oxygen vacancies in $Bi_2Zr_2O_7$ are directly related to the number of $O_2^-/O_2^{2-}$ active sites, and that weaker B–O bonds are the intrinsic factor for enhanced activity [8]. In addition, Wan et al. pointed out that the performance of high-temperature functional materials is not determined solely by their intrinsic structure, but is jointly governed by defect equilibrium, phase transitions, lattice disorder, and surface reaction kinetics [9,10]. To date, systematic comparative studies on the redox behavior and surface oxygen activity of Bi/Pr/Tb-based reducible $A_2B_2O_7$ systems with various sub-crystalline phase structures remain limited. Notably, there is a lack of understanding regarding the quantitative distinctions among the pyrochlore, solid solution, disordered defect fluorite and rare earth C-type phases. This work quantitatively establishes the 'structure-redox' relationship for these reducible systems by integrating Rietveld refinement, *in situ* Raman spectroscopy, and XPS, thereby addressing the aforementioned research gap.

We have systematically studied the preparation methods and structural identification strategies of $A_2B_2O_7$ composite oxides with varying sub-crystal phase structures and polymorphs [11]. Our findings indicate that Raman spectroscopy is the most effective technique for identifying their sub-crystal phase structures and lattice disorder [11]. Furthermore, we synthesized a series of non-reducible $A_2B_2O_7$ composite oxides using the glycine-nitrate combustion method, systematically exploring the influence of different lattice disorders and sub-crystal phase structures on the surface reactive oxygen sites, and identifying the types of active oxygen species [12]. Building upon this research foundation, we synthesized a series of reducible $A_2B_2O_7$ (where A = Bi, Pr, Tb; B = Ti, Sn, Zr, Ce) compounds using the citric acid sol-gel method. Through various characterization methods, the factors influencing their redox behavior and

reactive oxygen sites were systematically investigated. This provides a theoretical basis for the application of $A_2B_2O_7$ composite oxides in oxygen-assisted thermal catalysis reactions. It is noteworthy that we did not synthesize pure-phase $Bi_2Ti_2O_7$ pyrochlore using the citric acid sol-gel method, as this method tends to produce the thermodynamically more stable $Bi_4Ti_3O_{12}$ instead of $Bi_2Ti_2O_7$ pyrochlore.

## 2. Materials and Methods

### *2.1. Sample Preparation*

All samples were prepared using the citric acid sol-gel method, employing the A-site ion precursors: $Bi(NO_3)_3{\cdot}5H_2O$, $Pr(NO_3)_3{\cdot}6H_2O$, and $Tb(NO_3)_3{\cdot}6H_2O$, alongside the B-site ion precursors: $Ti(OC_4H_9)$, $SnC_2O_4$, $ZrO(NO_3)_2{\cdot}2H_2O$, and $Ce(NO_3)_3{\cdot}6H_2O$. The precursors were dissolved in deionized water at a molar ratio of A-site ion to B-site ion to citric acid of 1:1:1.2, and the mixture was stirred thoroughly. The resulting solution was evaporated in a water bath at 80 °C to yield a dry gel, which was subsequently aged in an oven at 130 °C for 12 h. Following this, the sample was ignited in an air atmosphere at 300 °C to remove the citric acid. For the Bi-based samples, high-temperature calcination may lead to the loss of Bi; therefore, these samples were calcined at 600 °C for 4 h. In contrast, the powders from the other samples were calcined at 800 °C in an air atmosphere for 4 h. Notably, to prevent the hydrolysis of $Bi^{3+}$ and $Ti^{4+}$ ions, $Bi(NO_3)_3{\cdot}5H_2O$ and $Ti(OC_4H_9)$ were dissolved in a 30% dilute nitric acid solution. $SnC_2O_4$, on the other hand, required dissolution in a specific amount of 30% $H_2O_2$ initially. Following complete dissolution, the A-site ion precursor was added. The inclusion of $H_2O_2$ oxidizes $Sn^{2+}$ to $Sn^{4+}$, which is more soluble in water.

### *2.2. Sample Characterization*

Raman and *in situ* Raman tests were conducted using a Renishaw inVia Reflex spectrometer (Renishaw, Gloucester, UK) with a laser wavelength of 532 nm, equipped with a Linkam TS 1500 *in situ* cell (Linkam Scientific Instruments, Surrey, UK). X-ray diffraction (XRD) analysis of the sample was performed using a Bruker AXS D8 Focus X-ray diffractometer (Bruker AXS, Karlsruhe, Germany) operating at 40 kV and 30 mA, utilizing a copper target and Kα X-ray irradiation. XPS analysis was performed on a Thermo Fisher Scientific ESCALAB 250Xi system (Thermo Fisher Scientific, Waltham, MA, USA) equipped with a monochromatic Al Kα X-ray source. Both hydrogen temperature-programmed reduction ($H_2$-TPR) and oxygen temperature-programmed desorption ($O_2$-TPD) analyses were executed using an Auto Chem 2920, Micromeritics Instrument (Micromeritics Instrument Corporation, Norcross, GA, USA). Detailed sample pretreatment steps are provided in the corresponding sections of the main text, and specific sample characterization methods are outlined in the supplementary materials. The $^{18}O_2$-TPSR-MS experiments were carried out on a BelCat II apparatus (Microtrac MRB, Osaka, Japan) equipped with a BelMass quadrupole mass spectrometer (Microtrac MRB, Osaka, Japan), with a 1 mL sampling loop and the gas flow rate controlled at 30–60 mL/min. For specific sample characterization methods and instrument testing conditions, please refer to the supporting materials.

## 3. Results and Discussion

### *3.1. Sample Structure and Phase*

We first utilized Raman spectroscopy, which is highly sensitive to the sub-crystal structure of $A_2B_2O_7$ composite oxides [11], to identify the bulk phase structure and lattice disorder of these samples. As illustrated in the Figure 1a, the Raman bands observed for $Bi_2Sn_2O_7$ in the range of 200–320 $cm^{-1}$ are attributed to the bending vibrations of O–Bi–O and O–Sn–O, as well as the stretching of the Bi–$SnO_6$ structure. The wavenumbers at 400, 506, and 532 $cm^{-1}$ correspond to O motion in $SnO_6$ polyhedra ($F_{2g}$), Bi–O′ stretching, and O′-vacancy stretching ($A_{1g}$), respectively [13]. These characteristic peaks are

consistent with the pyrochlore-type structure. It should be noted that $Bi_2Sn_2O_7$ exists in three polymorphic phases: monoclinic α-phase, face-centered cubic β-phase, and cubic pyrochlore γ-phase. The γ-cubic pyrochlore phase is stable only above 600 °C, while the room-temperature stable phase is the α-monoclinic phase. In addition, combined with the subsequent XRD Rietveld refinement results, it is further concluded that $Bi_2Sn_2O_7$ adopts the α-phase crystal form at room temperature. For $Bi_2Zr_2O_7$, the wavenumbers at 260, 448, and 597 $cm^{-1}$ are assigned to the external mode of vibration, pyrochlore microdomain, and the $F_{2g}$ mode of the Zr-based disordered defect fluorite phase [14], respectively, suggesting a disordered defect fluorite phase for $Bi_2Zr_2O_7$. In the case of $Bi_2Ce_2O_7$, the Raman bands at 312, 454, 535, and 590 $cm^{-1}$ correspond to the random distribution of metal cations in the sub-lattice, the $F_{2g}$ mode, the oxygen vacancies, and the $MO_8$-type complex of the Ce-based solid solution [15,16].

As displayed in Figure 1b, the complex Raman bands for $Pr_2Ti_2O_7$, including the Pr–O stretching vibration in the range of 110–460 $cm^{-1}$, the vibration of the distorted $TiO_6$ octahedron in the range of 500–600 $cm^{-1}$, and the Ti–O bond stretching vibrations located at approximately 785 and 810 $cm^{-1}$, are characteristic of the monoclinic layered perovskite structure [17]. In the case of $Pr_2Sn_2O_7$, the Raman bands observed at 300, 329, 391, 500, and 530 $cm^{-1}$ can be attributed to the $E_g$, $F_{2g}$, $F_{2g}$, $A_{1g}$, and $F_{2g}$ modes, respectively [18], indicating that $Pr_2Sn_2O_7$ possesses a pyrochlore phase. As demonstrated in Figure 1c, the Raman bands for $Tb_2Ti_2O_7$ are observed at 212, 305, 520, 590, and 720 $cm^{-1}$, corresponding to the $F_{2g}$, $E_g$ + $F_{2g}$, $F_{2g}$, $A_{1g}$, and $F_{2g}$ modes, respectively [19]. This observation is also consistent with a pyrochlore phase. In contrast, the Raman bands of $Tb_2Sn_2O_7$ are comparable to those of $Pr_2Sn_2O_7$; however, the peak widths are broader, and the intensities of several peaks are reduced, indicating a disordered pyrochlore crystal phase structure. The wavenumbers at 308, 324, 415, 507, and 533 $cm^{-1}$ correspond to the $E_g$, $F_{2g}$, $F_{2g}$, $A_{1g}$, and $F_{2g}$ modes [20], respectively.

In the case of $Pr_2Zr_2O_7$, similar to $Bi_2Zr_2O_7$, Raman modes are observed at 125, 306, and 620 $cm^{-1}$. These modes correspond to external vibrational frequencies, the pyrochlore microdomain, and the $F_{2g}$ mode associated with the disordered defect fluorite phase, respectively [14]. Compared to $Pr_2Zr_2O_7$, $Tb_2Zr_2O_7$ only shows a broader $F_{2g}$ mode. The relatively broader $F_{2g}$ band suggests a higher degree of local structural heterogeneity, which may arise from lattice distortion, cation disorder, or reduced crystallite size, among other factors. Literature reports suggest that the ionic radius ratio of $r_{Pr}/r_{Zr}$ and $r_{Tb}/r_{Zr}$ falls within the range for forming disordered defect fluorite [21,22]. The research results also demonstrate its disordered defect fluorite crystalline structure.

For $Pr_2Ce_2O_7$, the band with a wavenumber below 200 $cm^{-1}$ is attributed to the random distribution of positive ions in the oxygen ion sites [23]. The bands at 446 and 572 $cm^{-1}$ correspond to the $F_{2g}$ mode and the oxygen vacancy mode of the disordered defect fluorite phase, respectively [23]. For $Tb_2Ce_2O_7$, the Raman bands located at 150 $cm^{-1}$, 475 $cm^{-1}$, and 605 $cm^{-1}$ further indicate its structural consistency with the disordered defect fluorite phase. Compared to the prominent and sharp $F_{2g}$ peak of $Bi_2Ce_2O_7$, the $F_{2g}$ peaks of $Pr_2Ce_2O_7$ and $Tb_2Ce_2O_7$ are broader. Specifically, the $F_{2g}$ peak of $Pr_2Ce_2O_7$ shifts to a lower wavenumber of 445 $cm^{-1}$, while the $F_{2g}$ peak of $Tb_2Ce_2O_7$ shifts to a higher wavenumber of 472 $cm^{-1}$. Furthermore, neither $Pr_2Ce_2O_7$ nor $Tb_2Ce_2O_7$ exhibit $MO_8$-type complexes, and their Raman peaks corresponding to oxygen vacancies display symmetrical peak shapes. Thus, these findings support their classification as disordered defect fluorite crystal phases, combined with the absence of superstructural peaks in XRD. In addition, the lattice parameters obtained from subsequent XRD Rietveld refinement also support this conclusion. For Ce-based compounds, we utilize the $A_{OV}/A_{F2g}$ ratio of the integrated areas corresponding to oxygen vacancies and the $F_{2g}$ peaks to estimate the relative oxygen-vacancy content. The results demonstrate that the oxygen vacancy concentrations follow the order: $Tb_2Ce_2O_7$ (2.69) > $Pr_2Ce_2O_7$ (2.03) > $Bi_2Ce_2O_7$ (0.48).

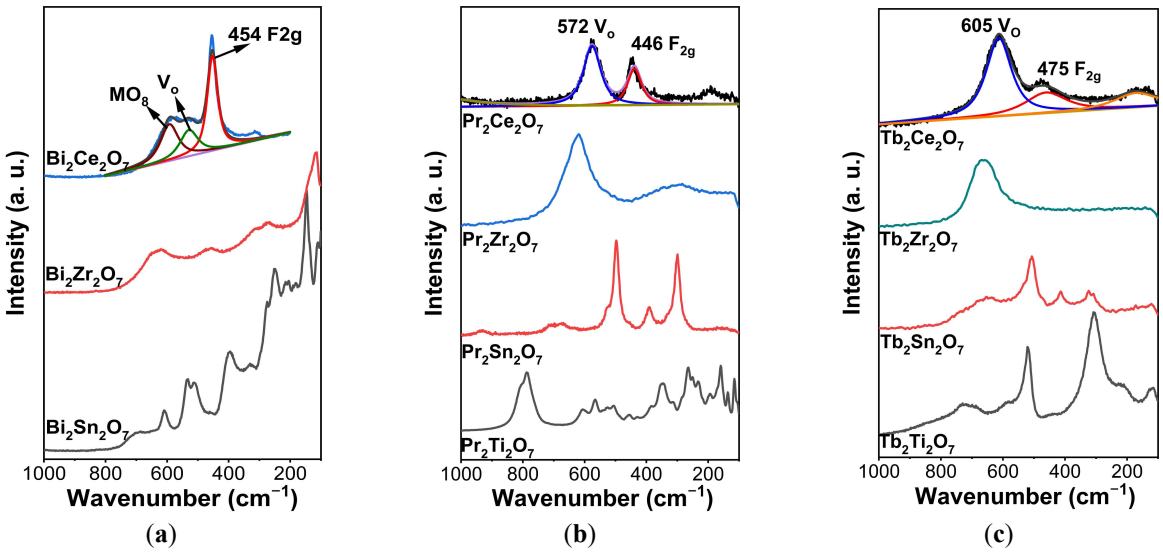



**Figure 1.** Raman spectra of the samples. (**a**) $Bi_2B_2O_7$ (B = Sn, Zr, Ce), (**b**) $Pr_2B_2O_7$ (B = Ti, Sn, Zr, Ce) and (**c**) $Tb_2B_2O_7$ (B = Ti, Sn, Zr, Ce).

XRD was utilized to further elucidate the crystal phase structures of the samples, as depicted in Figure 2a–c). With the exception of $Bi_2Zr_2O_7$, $Pr_2Zr_2O_7$, $Tb_2Zr_2O_7$, $Pr_2Ce_2O_7$, and $Tb_2Ce_2O_7$, for which standard reference cards are unavailable, the standard cards for the remaining samples—namely $Bi_2Sn_2O_7$, $Bi_2Ce_2O_7$, $Pr_2Ti_2O_7$, $Pr_2Sn_2O_7$, $Tb_2Ti_2O_7$, and $Tb_2Sn_2O_7$—are consistent with their respective standard cards (Jade 9, PDF#$Bi_2Sn_2O_7$: 97-008-6847, PDF#$Bi_2Ce_2O_7$: 97-018-4202, PDF#$Pr_2Ti_2O_7$: 97-008-3847, PDF#$Pr_2Sn_2O_7$: 97-008-2957, PDF#$Tb_2Ti_2O_7$: 97-015-9781, and PDF#$Tb_2Sn_2O_7$: 97-015-9786). For $Bi_2Zr_2O_7$, $Pr_2Zr_2O_7$, $Tb_2Zr_2O_7$, $Pr_2Ce_2O_7$, and $Tb_2Ce_2O_7$, the absence of characteristic diffraction peaks corresponding to the (331) and (511) crystal planes, with 2θ angles at 36.9° and 44.5° [11,24], further supports the conclusion that these compounds possess a disordered defect fluorite structure. Furthermore, no characteristic diffraction peaks of impurities were observed. Furthermore, no diffraction peaks attributable to crystalline impurity phases were detected within the detection limit of XRD, suggesting the absence of detectable crystalline impurity phases within the detection limit of XRD. To examine the reliability of the structural data, XRD Rietveld refinement of all samples was performed using HighScore X'Pert Plus software (GSAS 1) [25]. The lattice parameters of these samples were obtained by XRD Rietveld refinement (Figures S1–S3), and the results are presented in Table 1. Notably, with the exception of $Bi_2Sn_2O_7$ and $Pr_2Ti_2O_7$, which exhibit a monoclinic phase, all other samples are in a cubic phase. The lattice parameters of $Bi_2Sn_2O_7$ are 10.696. Whereas $Pr_2Ti_2O_7$ are a = 7.718 Å, b = 5.488 Å, c = 13.021 Å; α = 90°, β = 98.6°, γ = 90°.

For comparison, we synthesized A-site and B-site metal ion oxides using the same method, with their XRD results illustrated in Figure S4a,b. Notably, no diffraction peaks attributable to crystalline impurity phases were detected within the detection limit of XRD in any of the samples, indicating that the synthesized products are predominantly phase-pure. The XRD diffraction peaks of all metal oxides correspond with the standard reference cards (jade 9 PDF# $Bi_2O_3$: 00-014-0699, PDF# $Pr_6O_{11}$: 00-042-1121, PDF# $Tb_4O_7$: 00-013-0387, PDF# $TiO_2$: 00-021-1276, PDF# $SnO_2$: 00-041-1445, PDF# $ZrO_2$: 00-013-0307, PDF# $CeO_2$: 00-004-0593), indicating that no crystalline impurity phases were detected by XRD for the synthesized A-site and B-site metal oxides. Specifically, $Bi_2O_3$ is identified as belonging to the α-$Bi_2O_3$ crystalline phase, while $Pr_6O_{11}$ and $Tb_4O_7$ are classified within the defect fluorite phase. Furthermore, $TiO_2$ and $SnO_2$ are confirmed to be in the rutile phase, $ZrO_2$ is identified as being in the baddeleyite crystalline phase, and $CeO_2$ is classified as belonging to the fluorite crystalline phase.

**Table 1.** The physico-chemical properties of the samples.

| Samples | Crystalline Phases | Lattice Parameters * | | Specific Surface Areas ($m^2/g$) ** |
|---|---|---|---|---|
| | | a = b = c (Å) | α = β = γ (°) | |
| $Bi_2Sn_2O_7$ | Pyrochlore | 10.696 | 90 | 1.03/1.00 |
| $Bi_2Zr_2O_7$ | Fluorite | 5.348 | 90 | 0.97/1.00 |
| $Bi_2Ce_2O_7$ | Solid solution | 5.493 | 90 | 1.01/1.00 |
| $Pr_2Ti_2O_7$ | Perovskite | a = 7.718, b = 5.488 c = 13.021 | α = 90, β = 98.6, γ = 90 | 1.01/1.00 |
| $Pr_2Sn_2O_7$ | pyrochlore | 10.606 | 90 | 1.03/1.00 |
| $Pr_2Zr_2O_7$ | Fluorite | 5.304 | 90 | 0.98/1.00 |
| $Pr_2Ce_2O_7$ | Fluorite | 5.404 | 90 | 0.96/1.00 |
| $Tb_2Ti_2O_7$ | Ordered pyrochlore | 10.163 | 90 | 1.03/1.00 |
| $Tb_2Sn_2O_7$ | pyrochlore | 10.437 | 90 | 1.02/1.00 |
| $Tb_2Zr_2O_7$ | Fluorite | 5.230 | 90 | 0.98/1.00 |
| $Tb_2Ce_2O_7$ | Fluorite | 5.355 | 90 | 1.01/1.00 |

* Obtained from Rietveld refinement; ** Obtained by XPS.

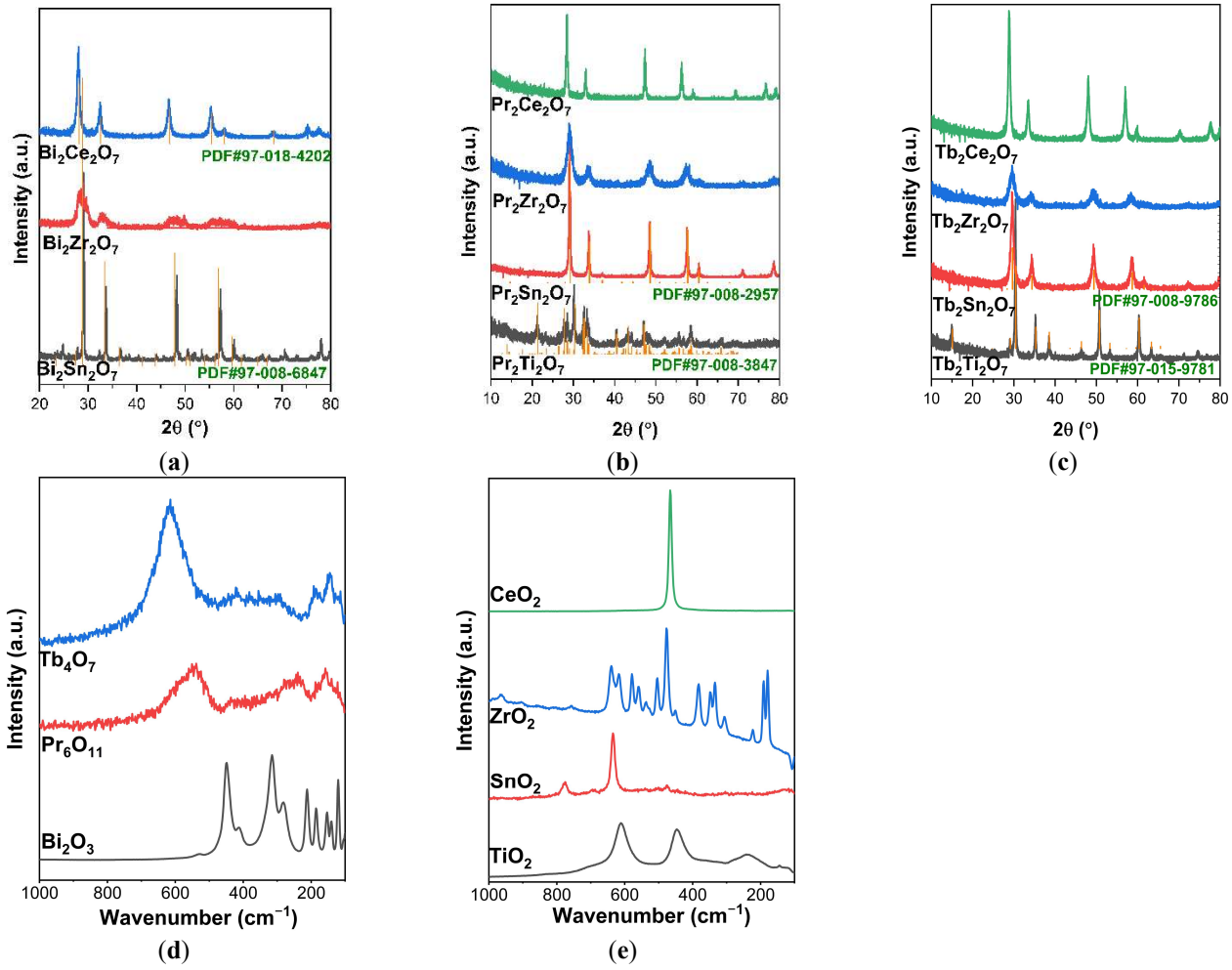



**Figure 2.** The orange lines in the figures correspond to the standard cards (PDF). XRD patterns (**a**–**c**) and Raman spectra (**d**,**e**) of the samples. (**a**) $Bi_2B_2O_7$ (B = Sn, Zr, Ce), (**b**) $Pr_2B_2O_7$ (B = Ti, Sn, Zr, Ce) and (**c**) $Tb_2B_2O_7$ (B = Ti, Sn, Zr, Ce). (**d**) Raman spectra of A-site metal oxides, (**e**) Raman spectra of B-site metal oxides.

Raman spectroscopy was employed to characterize the structures of A-site and B-site ionic oxides. As shown in Figure 2d, the Raman peaks for $Bi_2O_3$ appear at 116, 136, 150, 182, 208, 278, 312, 410, 446, and 526 $cm^{-1}$, This assignment is in good agreement with literature reports for α-$Bi_2O_3$ [26]. $Pr_6O_{11}$ and $Tb_4O_7$ exhibit similar Raman bands. The band around 585 $cm^{-1}$ is associated with distortions in the lattice and

$MO_8$ complexes ($A_{1g}$). Raman bands within the range of 250–400 $cm^{-1}$ are classified as second-order features due to their lower wavenumbers [27]. As illustrated in Figure 2e, the Raman peaks for $TiO_2$ are located at 243, 441, and 610 $cm^{-1}$, suggesting its identification as rutile-type $TiO_2$ [28]. For $SnO_2$, a band observed at 630 $cm^{-1}$ corresponds to the $A_{1g}$ mode, along with additional bands at 773 $cm^{-1}$ and 472 $cm^{-1}$ corresponding to the $B_{2g}$ and $E_g$ modes, respectively [29]. These characteristic bands demonstrate that $SnO_2$ is in the rutile crystal phase [29]. The $ZrO_2$ sample exhibits clearly defined peaks, with intense ones at 178, 189, and 476 $cm^{-1}$, characteristic of the monoclinic phase. Furthermore [30], three additional bands at 115 and 118 $cm^{-1}$ (doublets) and 753 $cm^{-1}$ have been identified as fundamental modes, contributing to the overall list of Raman-active vibrations for m-$ZrO_2$ [30]. For $CeO_2$, the characteristic $F_{2g}$ mode attributed to the fluorite structure is clearly observed at 465 $cm^{-1}$ [31]. The Raman results further confirm the successful synthesis of these pure-phase metal oxides.

### *3.2. Surface Analysis*

XPS spectra were utilized to investigate the surface properties of the reducible $A_2B_2O_7$ composite oxides and their corresponding metal oxides. As illustrated in Figure 3a, the binding energies at 158.8 eV and 164.1 eV correspond to Bi $4f_{7/2}$ and Bi $4f_{5/2}$, respectively, confirming that the oxidation state of Bi is +3 [32]. The binding energies depicted in Figure 3b, located at 932.6 eV and 953.0 eV, are associated with the peaks of Pr $3d_{5/2}$ and Pr $3d_{3/2}$, indicating that Pr is in the +4 oxidation state [33]. The satellite peaks are attributed to $Pr^{3+}$ species [33], and the content of $Pr^{3+}$ was calculated based on their integrated areas, as detailed in Table 2. It is evident that the disordered defect fluorite structure, characterized by a high degree of lattice disorder, contains a low concentration of $Pr^{4+}$ cations and a high concentration of $Pr^{3+}$ cations. As shown in Figure 3c, the binding energies at 1243, 1251, and 1278 eV can be attributed to $Tb^{4+}$ cations [34], while the binding energies at 1238, 1241, 1274, and 1276 eV correspond to $Tb^{3+}$ cations [34]. Similarly, the content of $Tb^{3+}$ was calculated based on its integrated areas and is presented in Table 2. The $Tb^{3+}$ content in the disordered defect fluorite phase is relatively low, whereas the $Tb^{4+}$ content in the structurally ordered pyrochlore phase is higher.

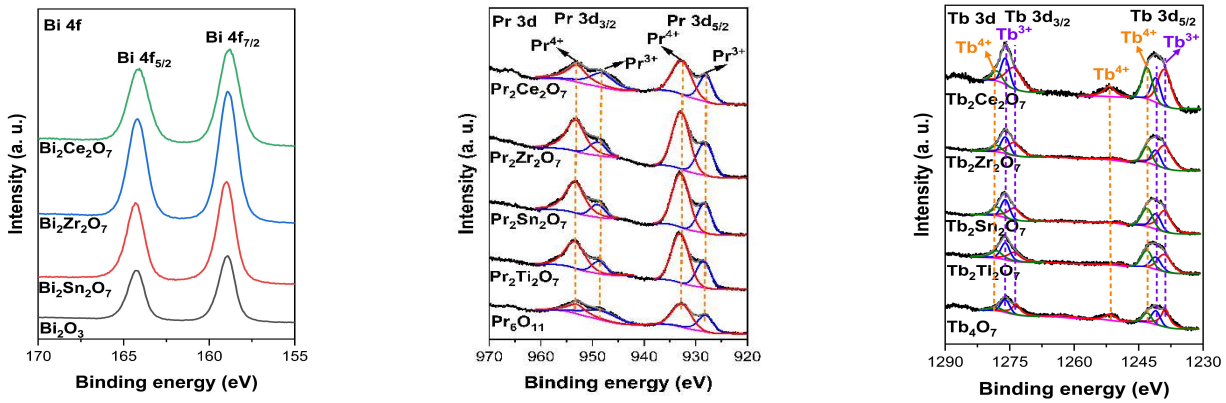



**Figure 3.** XPS spectra of the A-site elements of the samples. (**a**) Bi 4f, (**b**) Pr 3d and (**c**) Tb 3d.

As illustrated in Figure 4a, the peaks at 458.1 eV and 464.0 eV correspond to the binding energies of Ti $2p_{3/2}$ and Ti $2p_{1/2}$, confirming that Ti is in the +4 oxidation state [35]. As displayed in Figure 4b, the peaks at 486.3 eV and 494.8 eV, attributed to Sn $3d_{5/2}$ and Sn $3d_{3/2}$, indicate the typical $Sn^{4+}$ oxidation state [36]. As shown in Figure 4c, the characteristic peaks of Zr $3d_{3/2}$ and Zr $3d_{5/2}$ are observed at 181.6 eV and 183.9 eV, respectively, indicating that Zr is in the +4 oxidation state [33]. We deconvoluted the Ce 3d spectra of both pure $CeO_2$ and Ce-based samples into nine peaks based on binding energy and full width at half maximum (FWHM), as referenced in Reference [37], Where $Ce^{3+} = u + u_1 + v_0 + v_1$, $Ce^{4+} = u_2 + u_3 + v$

+ $v_2$ + $v_3$, and [$Ce^{3+}$(%)] = $Ce^{3+}$/($Ce^{3+}$ + $Ce^{4+}$) × 100%. The surface $Ce^{3+}$ content was calculated from the integral area of these peaks to indirectly reflect the concentration of surface oxygen defects [37].

**Table 2.** The content of $Pr^{3+}$, $Tb^{3+}$, and $Ce^{3+}$ on the surface of the sample.

| Sample | $Pr^{3+}$ (%) * | Sample | $Tb^{3+}$ (%) * | Sample | $Ce^{3+}$ (%) * |
|---|---|---|---|---|---|
| $Pr_6O_{11}$ | 42.5% | $Tb_4O_7$ | 59.8% | $CeO_2$ | 15.6 |
| $Pr_2Ti_2O_7$ | 28.0% | $Tb_2Ti_2O_7$ | 72.4% | $Bi_2Ce_2O_7$ | 25.1 |
| $Pr_2Sn_2O_7$ | 32.0% | $Tb_2Sn_2O_7$ | 75.2% | $Pr_2Ce_2O_7$ | 30.5 |
| $Pr_2Zr_2O_7$ | 37.8% | $Tb_2Zr_2O_7$ | 65.5% | $Tb_2Ce_2O_7$ | 36.2 |
| $Pr_2Ce_2O_7$ | 41.2% | $Tb_2Ce_2O_7$ | 62.1% | | |

* The content of each component was calculated from the integrated areas of the corresponding XPS peaks after deconvolution and peak fitting.

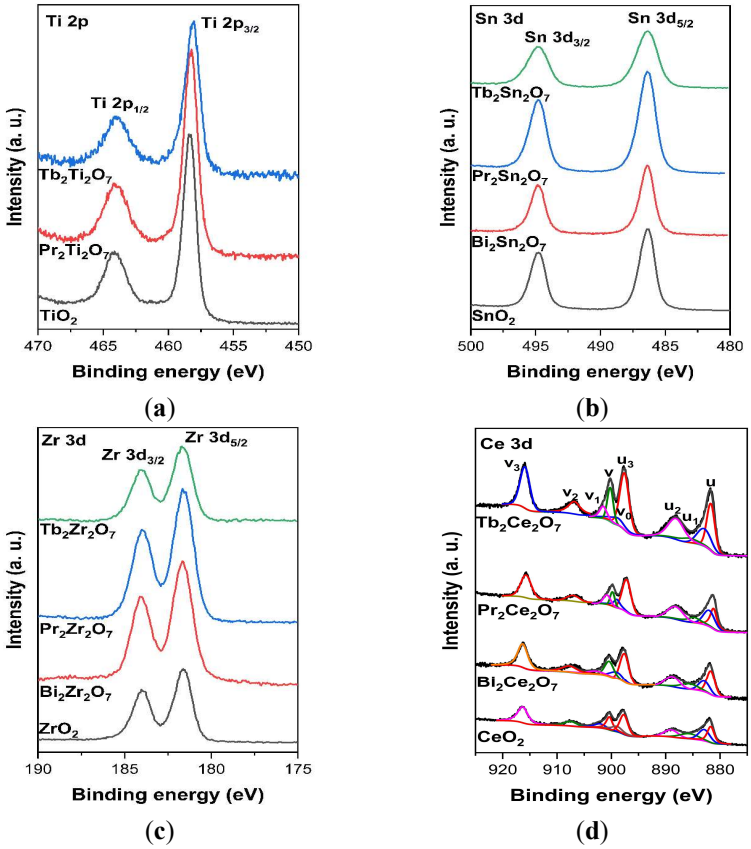



**Figure 4.** XPS spectra of the B-site elements of the samples. (**a**) Ti 2p, (**b**) Sn 3d, (**c**) Zr 3d and (**d**) Ce 3d.

The results are presented in Figure 4d and Table 2. The surface $Ce^{3+}$ content of the samples follows the order: $Tb_2Ce_2O_7$ > $Pr_2Ce_2O_7$ > $Bi_2Ce_2O_7$ > $CeO_2$, which aligns with the semi-quantitative Raman analysis. Additionally, we calculated the molar ratio of A-site ions to B-site ions on the surface of these samples, with the results listed in Table 1. It can be concluded that the molar ratio of A-site to B-site ions on the surface of all samples is close to the stoichiometric ratio of 1.00/1.00.

### *3.3. $H_2$-TPR and In Situ Raman Analysis*

$H_2$-TPR is employed to investigate the redox behavior of A-site and B-site ionic oxides, as well as reducible $A_2B_2O_7$ composite oxides. Initially, the sample undergoes pretreatment at 800 °C in a 10% $O_2$–Ar mixture to eliminate surface impurities and oxidize the surface of the sample. Subsequently, the sample is cooled to 100 °C in the same atmosphere and purged with high-purity Ar to remove any physically

adsorbed oxygen from the surface. The temperature is then raised at a rate of 10 °C/min until it reaches 800 °C. As illustrated in Figure 5a, $Bi_2O_3$ usually exists in the stable O–$Bi^{3+}$ form; when the temperature is raised under an $H_2$–Ar, $H_2$ reacts with lattice oxygen, removing oxygen atoms and generating metallic Bi. Therefore, the reduction temperatures for $Bi_2O_3$ at 562 °C and 693 °C correspond to the reduction of surface Bi–O bonds and partial bulk lattice oxygen, respectively [38]. The reduction behaviors of $Pr_6O_{11}$ and $Tb_4O_7$ are notably similar, with reduction peaks observed between 473 °C and 452 °C, which are attributed to the reduction of surface and a small amount of bulk $Pr^{4+}$ or $Tb^{4+}$ to $Pr^{3+}$ or $Tb^{3+}$ [39]. As illustrated in Figure 5b, the minor reduction peaks observed for $TiO_2$ and $ZrO_2$ can be attributed to the reduction of surface chemisorbed oxygen. In the case of $SnO_2$, the reduction peak observed at 622 °C corresponds to the reduction of tin dioxide to metallic tin. For $CeO_2$, the reduction peak at 760 °C is associated with the reduction of bulk lattice oxygen within $CeO_2$ [39]. To further analyze the reducibility of these oxides, the $H_2$ consumption of each oxide was calculated, as shown in Table S1. The total $H_2$ consumption order is $SnO_2 > Bi_2O_3 > Pr_6O_{11} > Tb_4O_7 > CeO_2 > ZrO_2 > TiO_2$. This indicates that $SnO_2$ and $Bi_2O_3$ exhibit higher $H_2$ consumption due to the deep reduction of $Sn^{4+}$ and $Bi^{3+}$ to the metallic state, whereas $Zr^{4+}$ and $Ti^{4+}$ in $ZrO_2$ and $TiO_2$ are almost irreducible within the tested temperature range.

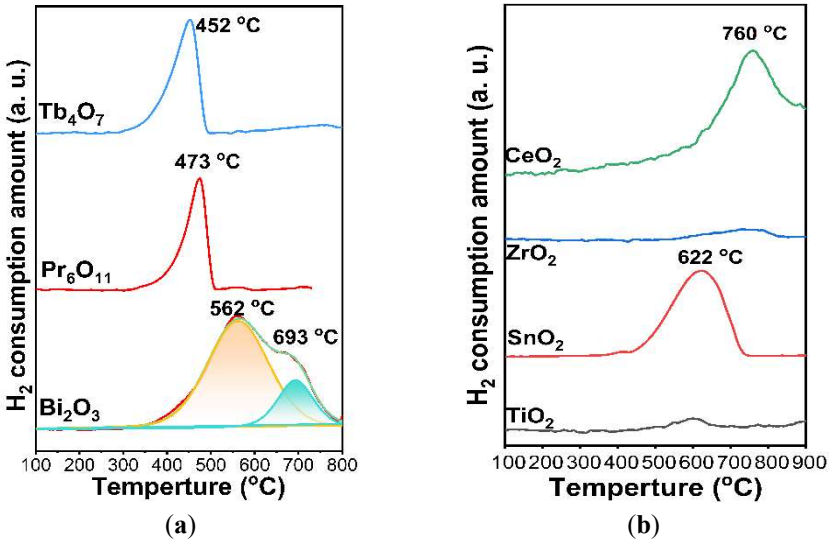



**Figure 5.** $H_2$-TPR profiles of the samples. (**a**) A-site metal oxides, (**b**) B-site metal oxides.

As shown in Figure 6a, for $Bi_2Sn_2O_7$, based on the reduction behaviors of pure $Bi_2O_3$ and $SnO_2$, $Bi_2Sn_2O_7$ exhibits two reduction peaks at 550 °C and 699 °C, where the low-temperature peak can be attributed to the reduction of $Bi^{3+}$ to $Bi^0$, and the high-temperature peak may be related to the reduction of $Sn^{4+}$ to $Sn^0$ or the reduction of lattice oxygen in the bulk $Bi_2O_3$. Compared to pure oxides, their reduction peak temperatures have increased. This may be attributed to the formation of a regular pyrochlore crystalline phase composite oxide, where the crystal lattice is protected, leading to an increase in the reduction temperature of each oxide. For $Bi_2Zr_2O_7$ and $Bi_2Ce_2O_7$, the peak with a reduction temperature ranging from 325–345 °C is attributed to the reduction of $Bi^{3+}$ to $Bi^0$. Compared with pure $Bi_2O_3$, the reduction peak temperature shifts by nearly 200 °C to lower values. This can be attributed to changes in the coordination environment of $Bi^{3+}$ [40]. The coordination number of α-$Bi_2O_3$ is 6 or 5, while the coordination number of $Bi^{3+}$ in the disordered defect fluorite structure and solid solution is 7 and 8, respectively.

A quantitative $H_2$ consumption analysis was conducted on Bi-based samples (Tables S1 and S2), revealing that the total $H_2$ consumption follows the order of $Bi_2Sn_2O_7 > Bi_2Zr_2O_7 > Bi_2Ce_2O_7$. Combined with the $H_2$-TPR results of the corresponding oxides, it indicates that the high $H_2$ consumption of $Bi_2Sn_2O_7$ is attributed to the dual reduction of $B^{3+}$ and $Sn^{4+}$, resulting in the formation of metallic Bi, metallic Sn, and $Sn_{0.95}Bi_{0.05}$ alloy. In contrast, the $H_2$ consumption of $Bi_2Zr_2O_7$ and $Bi_2Ce_2O_7$ is relatively low, primarily due

to the reduction of $Bi^{3+}$ to $Bi^0$, with $Zr^{4+}$ and $Ce^{4+}$ remaining in their oxide forms. This is consistent with the coexistence of metallic Bi and $ZrO_2$/$CeO_2$ observed in the XRD after reduction.

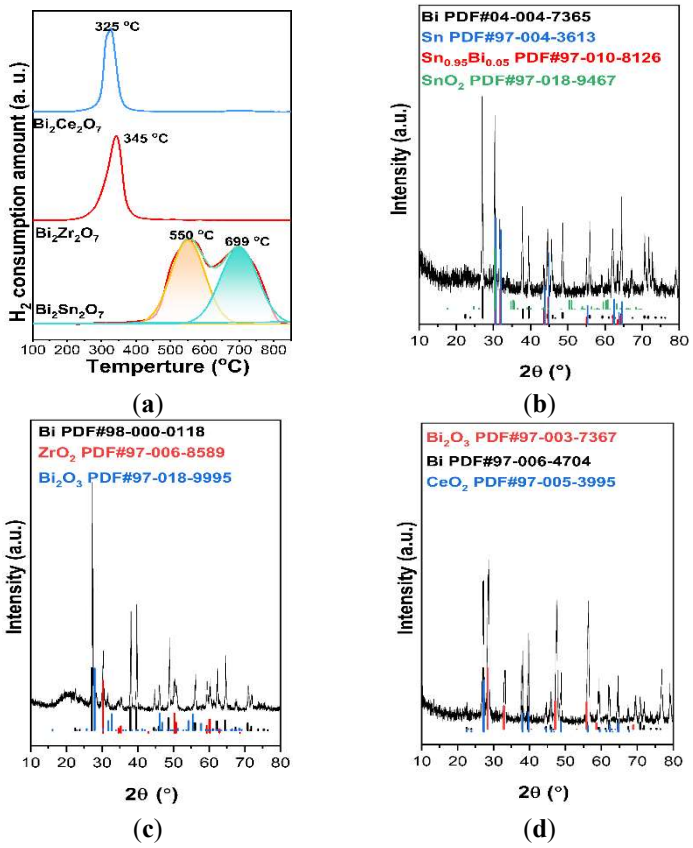



**Figure 6. (a)** $H_2$-TPR profiles of the Bi-based samples. XRD patterns of the Bi-based sample reduced by $H_2$–Ar at 800 °C. (**b**) $Bi_2Sn_2O_7$, (**c**) $Bi_2Zr_2O_7$ and (**d**) $Bi_2Ce_2O_7$.

The XRD results of all samples after reduction with a 10% $H_2$–Ar mixture at 800 °C are shown in Figure 6b–d. After reduction, the formation of metallic Bi can be observed in all samples. For $Bi_2Sn_2O_7$, the formation of $SnO_2$, metallic Sn, and $Sn_{0.95}Bi_{0.05}$ can also be observed, while a small amount of $Bi_2O_3$ can be observed in $Bi_2Zr_2O_7$ and $Bi_2Ce_2O_7$. In addition, the reduction of $Bi_2Zr_2O_7$ also generates tetragonal $ZrO_2$, and $Bi_2Ce_2O_7$ generates $CeO_2$. This indicates that the bulk structure of Bi-based samples will be destroyed as the temperature increases in a reducing gas atmosphere, and their reduction behavior is closely related to the A-site and B-site metal oxides. For example, $Bi_2O_3$ and $SnO_2$ can all be reduced; therefore, after high-temperature reduction, $Bi_2Sn_2O_7$ generates metallic Bi, metallic Sn, a $Sn_{0.95}Bi_{0.05}$ alloy, and $SnO_2$. As illustrated in Figure 7a, the monoclinic layered perovskite $Pr_2Ti_2O_7$ exhibits no reduction peaks, which is attributed to the non-reducibility of $Ti^{4+}$. For the ordered pyrochlore $Pr_2Sn_2O_7$, compared to the redox behavior of its respective A-site and B-site ionic oxides, reductions attributed to a small amount of surface or bulk $Pr^{4+}$ to $Pr^{3+}$ can be observed within the temperature range of 300–500 °C. Reduction peaks occurring at temperatures above 600 °C are ascribed to the reduction of surface $Sn^{4+}$ to metallic $Sn^0$. For the $Pr_2Zr_2O_7$ and $Pr_2Ce_2O_7$, the reduction peaks located at 385 and 430 °C are attributed to the reduction of a small amount of $Pr^{4+}$ to $Pr^{3+}$ on the surface or in the bulk. The quantitative results in Table S2 indicate that the total $H_2$ consumption follows the order $Pr_2Sn_2O_7 > Pr_2Zr_2O_7 \approx Pr_2Ce_2O_7 > Pr_2Ti_2O_7$. The significantly higher $H_2$ consumption of $Pr_2Sn_2O_7$ originates from the synergistic reduction of $Pr^{4+}$ and $Sn^{4+}$, whereas both $Pr_2Zr_2O_7$ and $Pr_2Ce_2O_7$ exhibit moderate and comparable $H_2$ consumption, primarily attributable to the reduction of $Pr^{4+}$ to $Pr^{3+}$. This observation aligns consistently with the findings from XPS results and *in situ* Raman spectroscopy analysis. Figure 7b shows that the formation of $SnO_2$ and metallic Sn can be observed

in $Pr_2Sn_2O_7$, while the XRD diffraction peaks of other samples do not exhibit significant changes. Due to the fact that XRD is less sensitive to disordered defect fluorite structures, solid solution structures, and rare earth C-type crystal phase structures compared to Raman spectroscopy, *in situ* Raman spectroscopy is required to identify whether these samples undergo crystal phase changes. For comparison, we also investigated their crystal phase changes under an inert, high-purity Ar gas atmosphere. The sample pretreatment method is the same as that for $H_2$-TPR. After cooling to room temperature in the *in situ* cell, introduce a 10% $H_2$–Ar mixed gas or high-purity Ar, and then maintain the temperature at 150 °C, 300 °C, 450 °C, 600 °C, and 750 °C for 15 min, respectively, while collecting relevant Raman spectra. Due to significant interference of thermal radiation on the Raman signals of some samples at 800 °C, all samples were sampled at a maximum temperature of 750 °C.

Figures S5–S7 demonstrates that all reducible $A_2B_2O_7$ compounds retain their respective sub-crystalline phase structures at varying temperatures in a high-purity Ar atmosphere under inert gas conditions. From the above, it can be seen that α-$Bi_2Sn_2O_7$ is a stable crystal phase at room temperature, and it transforms into β and γ phases as the temperature increases. The *in situ* Raman results show that in a high-purity Ar atmosphere, as the temperature increases, some Raman bands of $Bi_2Sn_2O_7$ not only vanish but also broaden markedly significantly, indicating that phase transitions/lattice distortions occur at high temperatures. This obversion suggests that it reversibly transforms into a high-symmetry phase (β/γ phase) above 600 °C. For other samples, under the same gas atmosphere, as the reaction temperature increases, their respective characteristic Raman spectra broaden without the disappearance of peaks. This can be attributed to the broadening caused by lattice thermal expansion, rather than lattice distortion or crystal phase change. Therefore, it can be concluded that, except for $Bi_2Sn_2O_7$, the other samples do not undergo high-temperature lattice distortion or crystal phase transition.

It is worth noting that for Bi-based samples, $Pr_2Sn_2O_7$ and $Tb_2Sn_2O_7$, due to the formation of metallic elements during the high-temperature reduction process, they volatilized onto the quartz plate of the *in situ* Raman cell, forming a layer of grayish-black spots, which affected the signal collection of the Raman spectra. Therefore, the *in situ* Raman results of these samples are not presented in $H_2$–Ar atmosphere. In fact, reliable conclusions can be drawn based on the XRD results, indicating that the Bi-based samples undergo structural collapse in a high-temperature $H_2$–Ar mixed gas atmosphere, generating metallic Bi and the related products described above. A small amount of Sn–O lattice oxygen on the surface or in the bulk phase of $Pr_2Sn_2O_7$ and $Tb_2Sn_2O_7$ is reduced to $SnO_2$ and metallic Sn.

Figure 7c indicates that no crystal phase change occurred in $Pr_2Ti_2O_7$ within the tested temperature range, as its corresponding Raman peaks matched those measured in a high-purity Ar atmosphere. As shown in the Figure 7d, at 450 °C, $Pr_2Zr_2O_7$ maintains its disordered defect fluorite structure. This indicates that under high-temperature reducing atmosphere, the lattice disorder degree further increases. Combined with the $H_2$-TPR results, this phenomenon may be related to the reduction of $Pr^{4+}$ to $Pr^{3+}$ in the surface or bulk phase. However, it should be noted that Raman peak broadening can also be influenced by other factors such as local lattice distortion, oxygen vacancy formation, or crystallite size effects. For $Pr_2Ce_2O_7$, it maintains a disordered defect fluorite structure at 450 °C. At 600 °C and 750 °C, characteristic Raman peaks attributed to rare earth C-type at 370 $cm^{-1}$ can be significantly observed [11,41]. Similar to $Pr_2Zr_2O_7$, $Pr^{4+}$ cation on its surface or in the bulk phase are reduced to $Pr^{3+}$, and the fluorite phase of $Pr_2Ce_2O_7$ transforms into a rare earth C-type crystalline phase. This also serves as good proof that the reduction of Ce–O lattice oxygen is not observed in $Pr_2Ce_2O_7$.

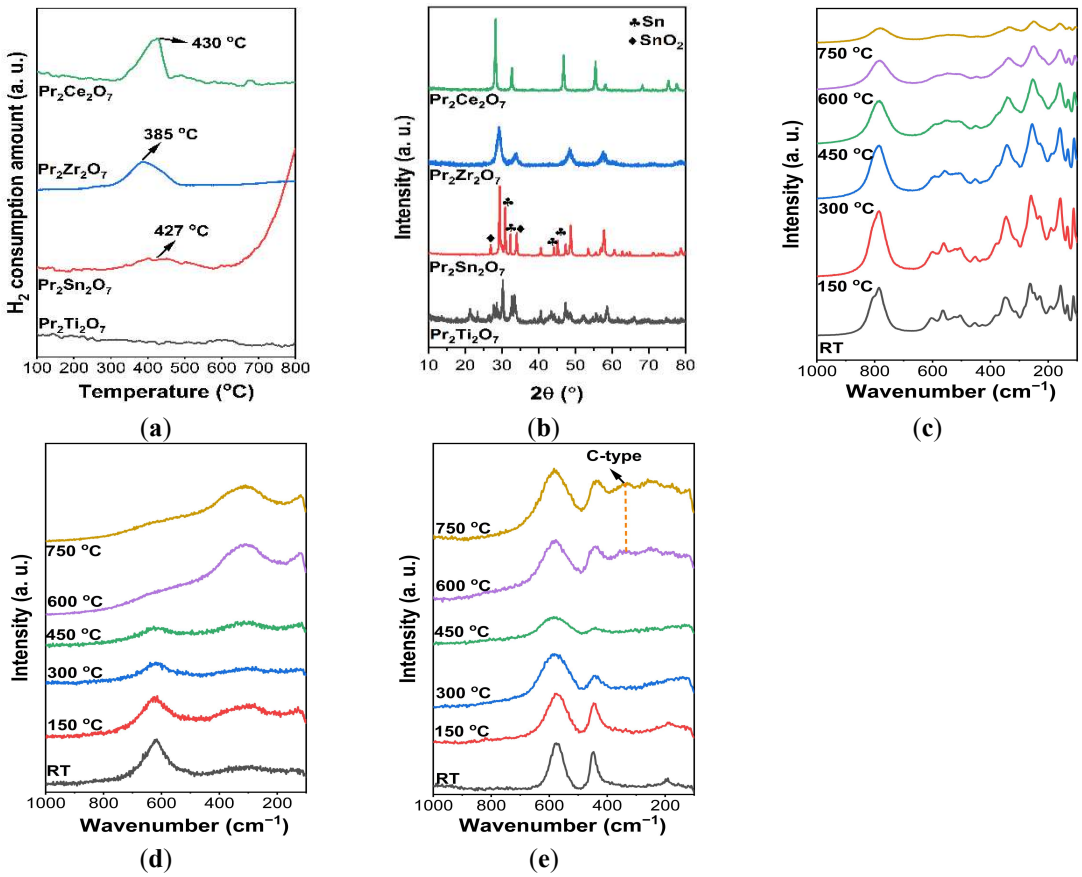



**Figure 7.** (**a**) $H_2$-TPR profiles of the Pr-based samples. (**b**) XRD patterns of the Pr-based sample reduced by $H_2$–Ar at 800 °C. *In situ* Raman spectra of the Pr-based samples. (**c**) $Pr_2Ti_2O_7$, (**d**) $Pr_2Zr_2O_7$, and (**e**) $Pr_2Ce_2O_7$.

The ordered pyrochlore $Tb_2Ti_2O_7$, as depicted in the Figure 8a shows no signs of reduction peaks. In contrast, the disordered pyrochlore $Tb_2Sn_2O_7$ demonstrates reductions linked to minimal amounts of surface or bulk $Tb^{4+}$ transitioning to $Tb^{3+}$ within the temperature span of 300–500 °C, especially when compared to the redox characteristics of its corresponding A-site and B-site ionic oxides. Additionally, reduction peaks that appear at temperatures exceeding 600 °C are attributed to the reduction of surface or bulk $Sn^{4+}$ into metallic $Sn^0$. For the compounds $Tb_2Zr_2O_7$ and $Tb_2Ce_2O_7$, reduction peaks at 405 and 432 °C correlate with the reduction of a small quantity of $Tb^{4+}$ to $Tb^{3+}$ either on the surface or within the bulk phase. The quantitative results in Table S2 indicate that the $H_2$ consumption of the Tb-based samples is similar to that of the Pr-based samples, also following the order of $Tb_2Sn_2O_7 > Tb_2Zr_2O_7 \approx Tb_2Ce_2O_7 > Tb_2Ti_2O_7$, which is consistent with their reduction pathways and the XPS and *in situ* Raman results. According to Figure 8b, all samples, except for the formation of metallic Sn can be observed in $Tb_2Sn_2O_7$, show negligible variations in XRD patterns post-reduction compared to their pre-reduction states. As displayed in Figure 8c–e, similar to the Pr-based sample, no significant crystal phase change was observed in $Pr_2Ti_2O_7$ within the reduction temperature range. In a high-temperature reducing atmosphere, the degree of lattice disorder in $Tb_2Zr_2O_7$ further increases. In the same atmosphere, at high temperatures, $Tb_2Ce_2O_7$ transitions from a disordered defect fluorite structure to an ordered rare-earth C-type structure.

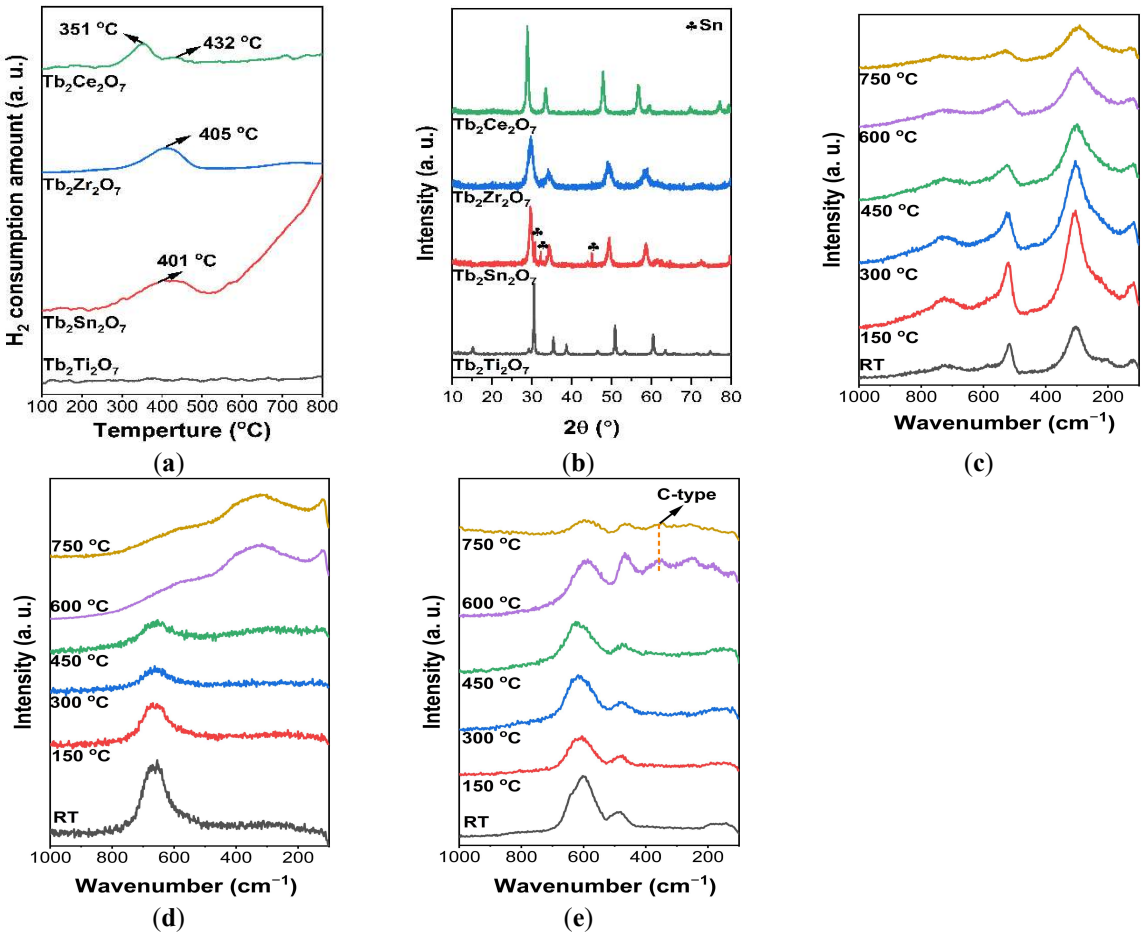



**Figure 8.** (**a**) $H_2$-TPR profiles of the Tb-based samples. (**b**) XRD patterns of the Tb-based sample reduced by $H_2$–Ar at 800 °C. *In situ* Raman spectra of the Tb-based samples. (**c**) $Tb_2Ti_2O_7$, (**d**) $Tb_2Zr_2O_7$, and (**e**) $Tb_2Ce_2O_7$.

### *3.4. $O_2$-TPD and $^{18}O_2$-TPSR-MS Analysis*

$O_2$-TPD was employed to investigate the surface-active oxygen sites of these reducible $A_2B_2O_7$ compounds. For comparative analysis, the corresponding A-site and B-site ionic oxides were also evaluated. The samples were initially treated in a 3% $O_2$–He mixture at 800 °C for 30 min, followed by cooling to 50 °C to facilitate adsorption for an additional 30 min. High-purity He was utilized to purge the surface, effectively removing physically adsorbed oxygen, after which the temperature was incrementally increased at a rate of 10 °C/min until reaching 800 °C. As illustrated in Figure 9a, no desorption peak of oxygen species was detected for $Bi_2O_3$. In contrast, $Pr_6O_{11}$ exhibited desorption peaks at 430, 520, 620, and above 800 °C. These peaks correspond to the desorption of lattice oxygen from $Pr_6O_{11}$ to $Pr_5O_9$, from $Pr_5O_9$ to $Pr_9O_{16}$, from $Pr_9O_{16}$ to $Pr_7O_{12}$, and from $Pr_7O_{12}$ to $Pr_6O_{10}$, respectively [42]. For $Tb_4O_7$, the desorption peaks located at 452 and 778 °C can be attributed to the desorption of lattice oxygen from $Tb_4O_7$ to $TbO_{1.818}$ and from $TbO_{1.818}$ to $TbO_{1.740}$, respectively [43].

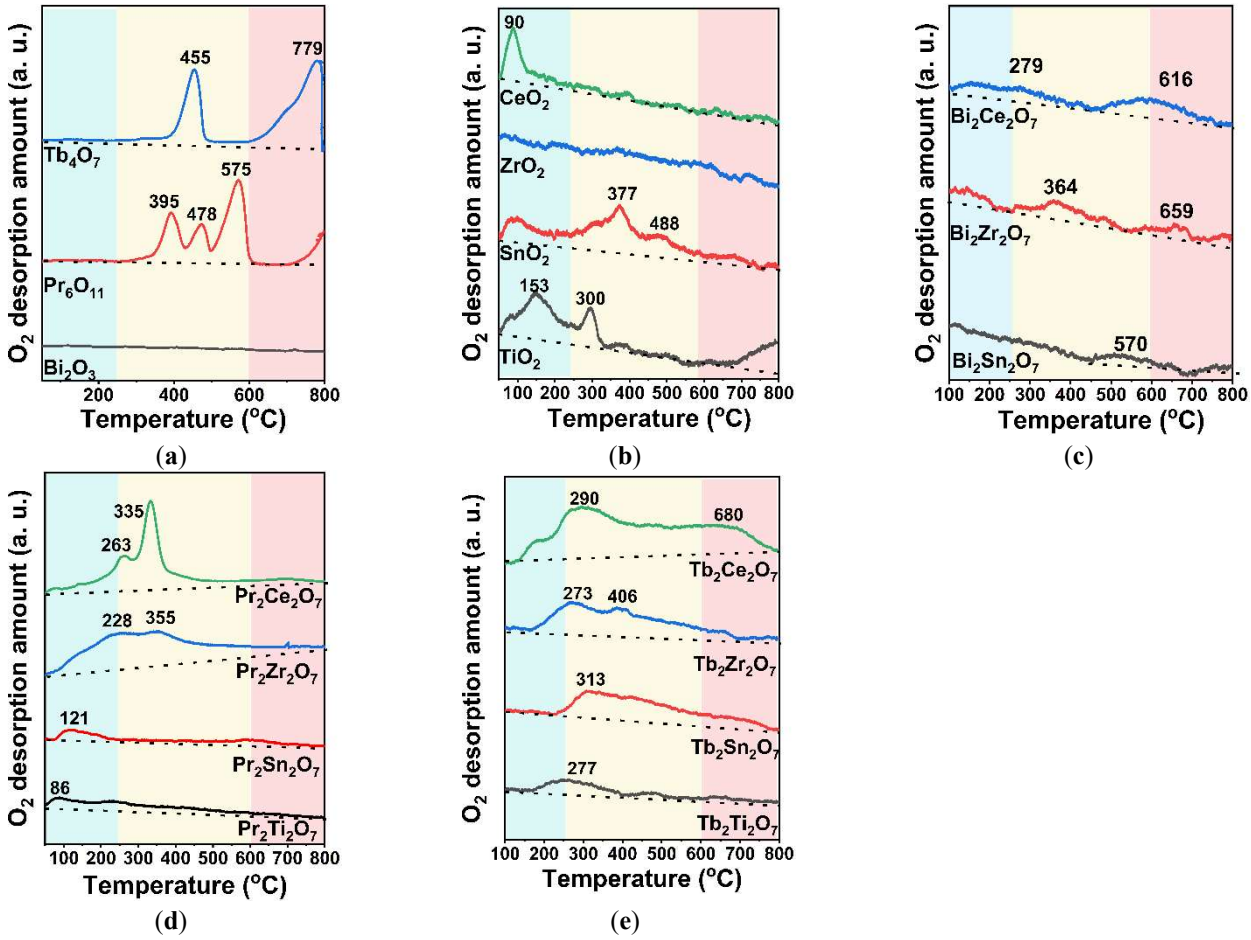



**Figure 9.** $O_2$-TPD profiles of the samples. (**a**) A-site metal oxides, (**b**) B-site metal oxides, (**c**) $Bi_2B_2O_7$ (B = Sn, Zr, Ce), (**d**) $Pr_2B_2O_7$ (B = Ti, Sn, Zr, Ce), and (**e**) $Tb_2B_2O_7$ (B = Ti, Sn, Zr, Ce). The desorption peaks are classified by temperature regions and highlighted with distinct shaded backgrounds: weakly bound oxygen (<250 °C, light blue), chemisorbed oxygen (250–600 °C, light yellow), and surface lattice oxygen (>600 °C, light red).

As shown in Figure 9b, the desorption temperature below 250 °C can be attributed to loosely bound oxygen species, while the desorption temperature ranging from 250 to 600 °C can be attributed to the desorption of chemisorbed oxygen species [44]. The desorption peak at temperatures above 600 °C can be attributed to the desorption of surface lattice oxygen [44]. For $TiO_2$ and $SnO_2$, the chemisorbed oxygen species is observed, while no such oxygen species desorption is observed for $ZrO_2$ and $CeO_2$.

For Bi-based samples, as shown in Figure 9c, due to their low intensity of active oxygen desorption peaks and relatively high noise, it is difficult to determine the desorption of their active oxygen species. Figure 9d shows that apart from the desorption of a small amount of weakly bound oxygen observed in $Pr_2Ti_2O_7$ and $Pr_2Sn_2O_7$, there is no indication of desorption of chemisorbed oxygen species. For $Pr_2Zr_2O_7$ and $Pr_2Ce_2O_7$, abundant desorption of oxygen species can be observed within the temperature range of 200–400 °C. Compared to the $O_2$-TPD profiles of A-site and B-site ionic oxides, it is evident that their active oxygen desorption behavior is similar to that of $Pr_6O_{11}$. Furthermore, the desorption peaks within this range do not exclude the possibility of including the desorption of chemisorbed oxygen species. As shown in Figure 9e, compared to Pr-based samples, Tb-based samples consistently exhibited a richer amount of active oxygen desorption across all structural types. Ordered pyrochlores and layered perovskites show only trace loosely bound oxygen (<250 °C), indicating rigid lattices constrain oxygen mobility. In contrast, disordered defect fluorites exhibit abundant chemisorbed oxygen (200–400 °C). The Tb-based sample contains a richer amount of chemisorbed oxygen than the corresponding Pr-based sample. Bi-based defect fluorites show negligible desorption due to the non-desorbable property of $Bi_2O_3$. These results demonstrate

that oxygen mobility follows the order: disordered-defect fluorite > ordered pyrochlore ≈ layered perovskite, confirming that lattice disorder and structural openness are the key factors governing oxygen mobility.

To further identify the oxygen species, four representative samples ($Bi_2Ce_2O_7$, $Tb_2Zr_2O_7$, $Bi_2Sn_2O_7$, $Pr_2Ti_2O_7$) were selected for $^{18}O_2$ isotope exchange experiments. Typically, 100 mg of the sample was activated at 800 °C in a 10% $O_2$–Ar gas mixture for 30 min, then cooled to 200 °C then purged under a high purity Ar for 15 min to remove physiosorbed oxygen. Subsequently, the atmosphere was switched to 10% $^{18}O_2$–Ar, and the temperature was raised to 800 °C at a heating rate of 10 °C/min, while recording the mass spectrometry signals of $m/z$ = 32 ($^{16}O^{16}O$), 34 ($^{16}O^{18}O$), and 36 ($^{18}O1^{8}O$). Research indicates that there are two mechanisms involved in the exchange between gas-phase $^{18}O_2$ and surface-active oxygen species on metal oxides as follows [45]:

$$^{18}O^{18}O\ (g) + {}^{16}O\ (s) \rightarrow {}^{16}O^{18}O\ (g) + {}^{18}O\ (s)\ \text{Simple hetero-exchange mechanism} \quad (1)$$

$$^{18}O^{18}O\ (g) + 2{}^{16}O\ (s) \rightarrow {}^{16}O^{16}O\ (g) + 2{}^{18}O\ (s)\ \text{Multiple hetero-exchange mechanism} \quad (2)$$

Mechanism (1) involves the exchange between gas-phase $^{18}O_2$ and monoatomic surface lattice oxygen $O^{2-}$, while Mechanism (2) involves the exchange between gas-phase $^{18}O_2$ and diatomic surface oxygen species such as $O_2^-$ or $O_2^{2-}$, which are catalyzed by oxygen vacancies and chemically adsorbed.

As shown in Figure 10, the results indicate that $A_2B_2O_7$ samples with different structural types exhibit significantly different behavior in $^{18}O_2$ exchange. The $^{16}O^{18}O$ signals of solid solution $Bi_2Ce_2O_7$ (Figure 10a) and disordered defect fluorite $Tb_2Zr_2O_7$ (Figure 10b) begin to rise markedly from 380 to 433 °C, whereas the onset temperatures of pyrochlore $Bi_2Sn_2O_7$ (Figure 10c) and layered perovskite $Pr_2Ti_2O_7$ (Figure 10d) are delayed to approximately 596 °C and 662 °C, respectively. This order is consistent with the ease of desorption of chemisorbed oxygen in $O_2$-TPD, indicating that an open lattice and a higher oxygen vacancy concentration facilitate oxygen activation and migration, while an ordered structure markedly suppresses oxygen exchange. In addition, the signal intensities of diatomic oxygen species ($O_2^-$, $O_2^{2-}$) are significantly higher than those of monoatomic lattice oxygen ($O^{2-}$), indicating that surface chemisorbed oxygen is the primary active species involved in exchange. Combined with the $O_2$-TPD results, it can be concluded that the desorption peaks in the range of 200–400 °C mainly correspond to the desorption and exchange of chemisorbed oxygen, while the signals at >600 °C more reflect the participation of surface lattice oxygen, further demonstrating that the disordered defect fluorite phase can activate and migrate surface oxygen species at low-to-medium temperatures, whereas pyrochlore and layered perovskite structures require higher temperatures to initiate oxygen exchange.

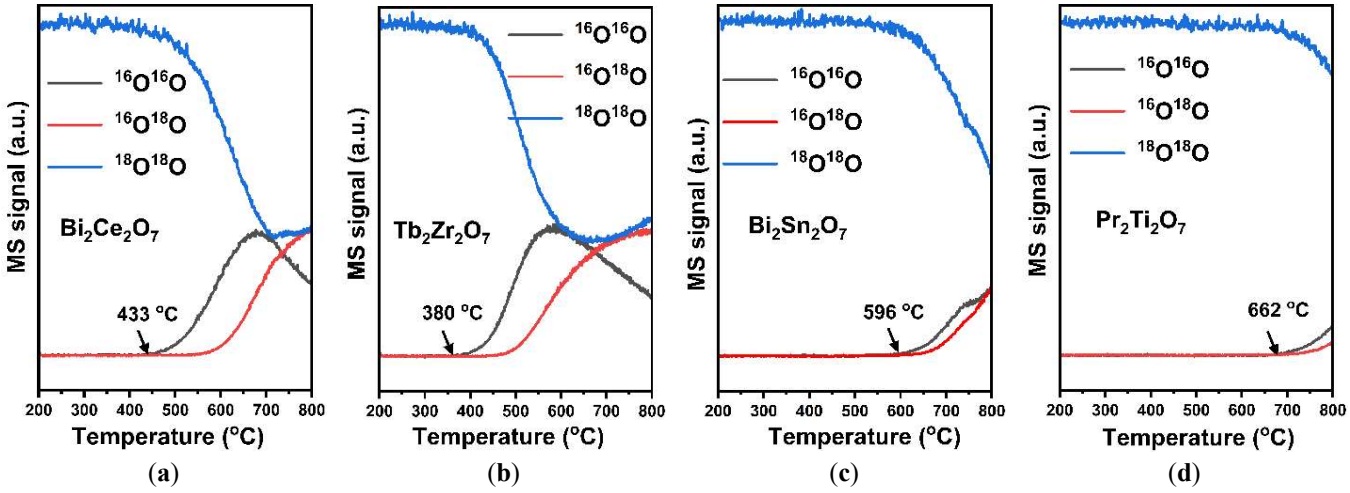



**Figure 10.** $^{18}O_2$-TPSR-MS profiles of the samples. (**a**) $Bi_2Ce_2O_7$, (**b**) $Tb_2Zr_2O$, (**c**) $Bi_2Sn_2O_7$, (**d**) $Pr_2Ti_2O_7$.

### *3.5. XPS O 1s Analysis*

XPS was employed to investigate the variations in surface chemisorbed oxygen species and surface lattice oxygen species in these reducible composite oxides. According to the binding energies located at 529.5 eV, 531.2 eV, and 533.0 eV, they are attributed to surface lattice oxygen $O^{2-}$, chemisorbed oxygen species, and bound $H_2O$, respectively [46]. The FWHM of each oxygen species is controlled to be within 1.8–2.2 eV. The XPS O 1s peaks of these samples are deconvoluted and fitted using a Lorentzian-Gaussian mixture function (L:G = 2:8). The $O_{ads}/O_{lat}$ ratio was used to semi-quantitative determine the content of surface chemisorbed oxygen species, and the results are shown in Figure 11a–c and Table 3. For Bi-based, Pr-based, and Tb-based samples, their $O_{ads}/O_{lat}$ ratios follow the order of $Bi_2Ce_2O_7 > Bi_2Zr_2O_7 > Bi_2Sn_2O_7$, $Pr_2Zr_2O_7 \approx Pr_2Ce_2O_7 > Pr_2Sn_2O_7 > Pr_2Ti_2O_7$ and $Tb_2Zr_2O_7 \approx Tb_2Ce_2O_7 > Tb_2Sn_2O_7 > Tb_2Ti_2O_7$, respectively.

Our preliminary research results indicate that when the sub-crystal phase structure and lattice disorder change, the amount of adsorbed oxygen species on the surface of $A_2B_2O_7$ composite oxides follows the order of disordered defect fluorite > rare earth C-type > disordered pyrochlore > ordered pyrochlore > layered perovskite [12,47]. In this series of reducible $A_2B_2O_7$ composite oxides, the same trend is still observed. This result suggests that, for the reducible $A_2B_2O_7$ compounds, the surface chemisorbed oxygen content correlates with the sub-crystalline phase structure and the lattice disorder degree, although additional factors may also contribute.

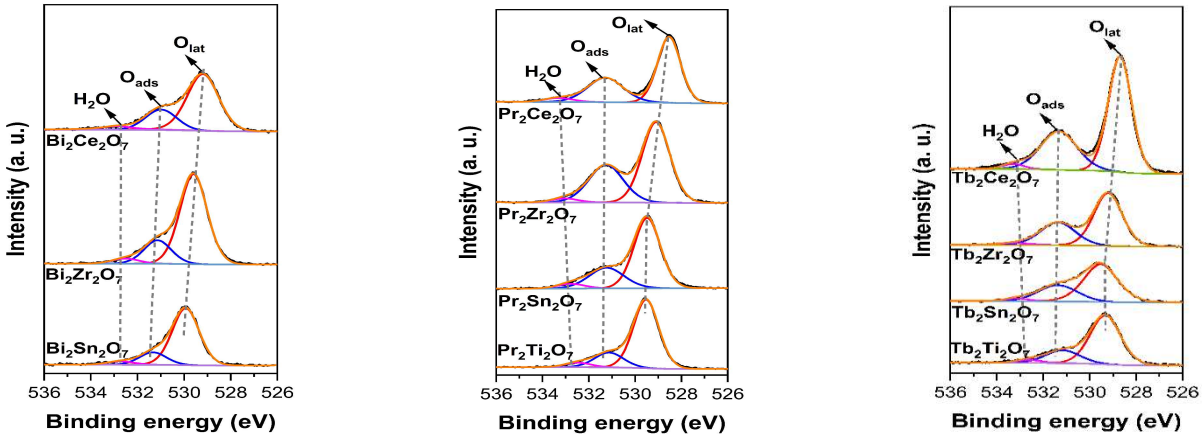



**Figure 11.** XPS O 1s results of the (**a**) Bi-based, (**b**) Pr-based and (**c**) Tb-based samples.

**Table 3.** The content of $O_{ads}/O_{lat}$ on the surface of the sample.

| Samples | $O_{ads}/O_{lat}$ | Samples | $O_{ads}/O_{lat}$ | Samples | $O_{ads}/O_{lat}$ |
|---|---|---|---|---|---|
| $Bi_2Sn_2O_7$ | 0.22 | $Pr_2Ti_2O_7$ | 0.25 | $Tb_2Ti_2O_7$ | 0.30 |
| $Bi_2Zr_2O_7$ | 0.26 | $Pr_2Sn_2O_7$ | 0.39 | $Tb_2Sn_2O_7$ | 0.48 |
| $Bi_2Ce_2O_7$ | 0.37 | $Pr_2Zr_2O_7$ | 0.55 | $Tb_2Zr_2O_7$ | 0.58 |
| - | - | $Pr_2Ce_2O_7$ | 0.51 | $Tb_2Ce_2O_7$ | 0.53 |

### *3.6. A Brief Discussion*

The above results indicate that for redox properties, the distribution of reduction products among the different Bi-based samples depends on the nature of the B-site cation, where $Sn^{4+}$ can be reduced to metallic Sn, while $Zr^{4+}$ and $Ce^{4+}$ remain in oxide. For Sn-based samples, $Pr_2Sn_2O_7$ and $Tb_2Sn_2O_7$, a small amount of metallic Sn is observed on the surface or in the bulk phase. Compared to their corresponding A-site or B-site ionic oxides, it can be found that $Bi_2O_3$ and $SnO_2$ are easily reduced, and thus the corresponding composite oxides are also easily reduced. For $Pr_2Ti_2O_7$ and $Tb_2Ti_2O_7$, Ti–O lattice oxygen is not easily reducible, in addition, XPS results indicate the presence of $Pr^{4+}$ and $Tb^{4+}$ on their surfaces. However, no

significant reduction from $Pr^{4+}$ to $Pr^{3+}$ is observed, which may be due to the relatively rigid layered perovskite and ordered pyrochlore crystal structures, forming lattice protection and thus preventing the observation of reduction peaks.

For $Pr_2Sn_2O_7$ and $Tb_2Sn_2O_7$, both of them exhibit the reduction of $Pr^{4+}$ to $Pr^{3+}$ and $Tb^{4+}$ to $Tb^{3+}$. Despite exhibiting ordered and disordered pyrochlore crystalline phases, respectively, with relatively rigid structures, the reduction of $Pr^{4+}$ and $Tb^{4+}$ is facilitated due to the relatively easy reduction of Sn-O lattice oxygen. For $Pr_2Zr_2O_7$ and $Tb_2Zr_2O_7$, their lattice disorder degree increases after high-temperature reduction. This can be attributed to the surface, or bulk $Pr^{4+}$ and $Tb^{4+}$ are completely reduced to $Pr^{3+}$ and $Tb^{3+}$, thus undergoing structural reconstruction at high temperatures to form a more disordered crystal structure. Although Ce–O bonds can be reduced at high temperatures, no reduction of Ce–O lattice oxygen was observed in $Pr_2Ce_2O_7$ and $Tb_2Ce_2O_7$. This is due to the formation of rare earth C-type crystal phase structures at high temperatures (>600 °C).

Similarly, the desorption of oxygen species is also influenced by the ionic oxides at the A-site and B-site, as well as the rigidity and looseness of the sub-crystalline phase structure. For example, in the layered perovskite structure with strong rigidity, such as the pyrochlore structures of $Pr_2Ti_2O_7$, $Pr_2Sn_2O_7$, $Tb_2Ti_2O_7$, and $Tb_2Sn_2O_7$, no desorption of surface lattice oxygen was observed. However, in the defect fluorite structures with relatively loose sub-crystalline phases [48], such as $Pr_2Zr_2O_7$, $Pr_2Ce_2O_7$, $Tb_2Zr_2O_7$, and $Tb_2Ce_2O_7$, a small amount of lattice oxygen desorption was shown. For Bi-based samples, since $Bi_2O_3$ does not exhibit desorbable lattice oxygen, no desorption of corresponding oxygen species was observed.

Regarding the chemisorbed oxygen species on the surfaces of these samples, the redox properties do not seem to exert additional influence. Instead, they are still influenced by the sub-crystalline phase structure and lattice disorder, specifically following the order of disordered defect fluorite > pyrochlore > layered perovskite. This indicates that the type of sub-crystalline phase structure and lattice disorder are fundamental factors that affect the content of chemisorbed oxygen species on their surfaces [49].

Research on the $La_2Sn_{1.8}TM_{0.2}O_7$ (TM = Mn, Fe, Co, Cu) system has confirmed that structural defects introduced by transition metal doping can significantly enhance low-temperature reducibility and oxygen vacancy concentration [50]. This is consistent with the trend observed in this work, where the disordered defect fluorite phase exhibits more abundant oxygen vacancies than the ordered pyrochlore phase. Recent studies have also shown that 10-component complex composition ceramics can undergo a reversible order-disorder transition from pyrochlore to disordered defect fluorite under reducing atmospheres [51]. This provides supporting evidence for the increased lattice disorder observed in $Pr_2Zr_2O_7$ under high-temperature reducing conditions in this work.

## 4. Conclusions

In this study, a series of reducible $A_2B_2O_7$ composite oxides was synthesized using a simple citric acid sol-gel method. Their redox behavior and active oxygen species were investigated in detail using various characterization techniques, and the following conclusions were drawn:

(1) As the temperature increases, in a reducing atmosphere, $Pr_2Zr_2O_7$ and $Tb_2Zr_2O_7$ exhibit an increase in lattice disorder, while $Pr_2Ce_2O_7$ and $Tb_2Ce_2O_7$ transition from a disordered defect fluorite to a rare earth C-type. These structural transitions are closely related to the reduction of $Pr^{4+}/Tb^{4+}$ to $Pr^{3+}/Tb^{3+}$.

(2) The oxygen mobility and the amount of surface chemisorbed oxygen are influenced by sub-crystalline structure and lattice disorder, rather than by redox properties. This influence follows the following order: disordered defect fluorite > ordered pyrochlore > layered perovskite. Structures with open defect fluorite structure and high disorder promote oxygen migration, while rigid ordered structures restrict oxygen migration.

## Supplementary Materials

The following supporting information can be found at: https://www.sciepublish.com/article/pii/1282, Figure S1: XRD Rietveld refinement spectra of the Bi-based samples. (a) $Bi_2Sn_2O_7$, (b) $Bi_2Zr_2O_7$ and (c) $Bi_2Ce_2O_7$, Figure S2: XRD Rietveld refinement spectra of the Pr-based samples. (a) $Pr_2Ti_2O_7$, (b) $Pr_2Sn_2O_7$, (c) $Pr_2Zr_2O_7$ and (d) $Pr_2Ce_2O_7$, Figure S3: XRD Rietveld refinement spectra of the Tb-based samples. (a) $Tb_2Ti_2O_7$, (b) $Tb_2Sn_2O_7$, (c) $Tb_2Zr_2O_7$ and (d) $Tb_2Ce_2O_7$, Figure S4: XRD patterns of the pure metal oxides. (a) A-site metal oxides, (b) B-site metal oxides, Figure S5: *In situ* Raman spectra of the Bi-based samples under high-purity Ar atmosphere. (a) $Bi_2Sn_2O_7$, (b) $Bi_2Zr_2O_7$ and (c) $Bi_2Ce_2O_7$, Figure S6: *In situ* Raman spectra of the Pr-based samples under high-purity Ar atmosphere. (a) $Pr_2Ti_2O_7$, (b) $Pr_2Sn_2O_7$, (c) $Pr_2Zr_2O_7$ and (d) $Pr_2Ce_2O_7$, Figure S7: *In situ* Raman spectra of the Tb-based samples under high-purity Ar atmosphere. (a) $Tb_2Ti_2O_7$, (b) $Tb_2Sn_2O_7$, (c) $Tb_2Zr_2O_7$ and (d) $Tb_2Ce_2O_7$, Table S1 Quantitative results of $H_2$-TPR of oxides, Table S2 Quantitative results of $H_2$-TPR of $Bi_2B_2O_7$, $Pr_2B_2O_7$ and $Tb_2B_2O_7$ (B=Ti, Sn, Zr, Ce), Table S3 Quantitative results of $O_2$-TPD.

## Statement of the Use of Generative AI and AI-Assisted Technologies in the Writing Process

During the preparation of this manuscript, the author used CITEXS and DEEPSEEK software to polish the English. After using this tool/service, the author(s) reviewed and edited the content as needed and take(s) full responsibility for the content of the published article.

## Author Contributions

Investigation, X.Y., W.R., Y.F. and L.M.; Validation, X.Y.; Visualization, X.Y.; Writing—Original Draft Preparation, X.Y.; Writing—Review and Editing, X.Y., J.X. and X.W.; Supervision, J.X.; Project Administration, J.X. and X.W.; Funding Acquisition, X.W.

## Ethics Statement

Not applicable.

## Informed Consent Statement

Not applicable.

## Data Availability Statement

Data will be made available on request.

## Funding

This research was supported by the National Natural Science Foundation of China (22462011, 22376090), the Natural Science Foundation of Jiangxi Province (20252BAC240720), and the Key Laboratory of Jiangxi Province for Environment and Energy Catalysis (20242BCC32041).

## Declaration of Competing Interest

The authors declare that they have no known competing financial interests or personal relationships that could have appeared to influence the work reported in this paper.

## References

1. Wang Z, Zhou G, Jiang D, Wang S. Recent development of $A_2B_2O_7$ system transparent ceramics. *J. Adv. Ceram.* **2018**, *7*, 289–306. DOI:10.1007/s40145-018-0287-z

2. Zhang S, Xu J, Wang X. The preparation, structure characterization and thermocatalytic chemistry of $A_2B_2O_7$ complex oxides in environment and energy reactions. *Sci. China Chem.* **2026**, *69*, 2230–2243. DOI:10.1007/s11426-025-3049-1
3. Wang C, Wang Y, Chen M, Liang D, Yang Z, Cheng W, et al. Recent advances during $CH_4$ dry reforming for syngas production: A mini review. *Int. J. Hydrogen Energy* **2021**, *46*, 5852–5874. DOI:10.1016/j.ijhydene.2020.10.240
4. Ai L, Wang Z, Cui C, Liu W, Wang L. Catalytic Oxidation of Soot on a Novel Active Ca-Co Dually-Doped Lanthanum Tin Pyrochlore Oxide. *Materials* **2018**, *11*, 653. DOI:10.3390/ma11050653
5. Yu X, Xu J, Wang X. Engineering functional perovskite and pyrochlore complex oxide catalysts. *Trends Chem.* **2026**, *8*, 616–629. DOI:10.1016/j.trechm.2026.07.002
6. Deng J, Chen P, Xia S, Zheng M, Song D, Lin Y, et al. Advances in Oxidative Coupling of Methane. *Atmosphere* **2023**, *14*, 1538. DOI:10.3390/atmos14101538
7. Xu J, Zhou J, Guo L, Ouyang R, Yu X, Wang X. Investigating the variation of oxygen vacancies in different sub-crystalline structures of $Ln_2Ce_2O_7$ (Ln = Pr, Nd) under different atmospheres via *in situ* Raman spectra. *J. Solid State Chem.* **2025**, *350*, 125517. DOI:10.1016/j.jssc.2025.125517
8. Zhang S, Feng X, Xu Z, Li Y, Wang P, Shen J, et al. The controlled engineering of surface oxygen defects on $Bi_2Zr_2O_7$ compounds for catalytic soot combustion by adjusting the preparation methods. *Phys. Chem. Chem. Phys.* **2024**, *26*, 974–984. DOI:10.1039/D3CP04104B
9. Huang J, Feng J, Yang M, Liu K, Hu B, Xu W, et al. High-Temperature-Resistant Mid-Infrared Capability for Extreme Energy Systems. *Nano-Micro Lett.* **2026**, *18*, 432. DOI:10.1007/s40820-026-02290-w
10. Zhu Z, Zhang H, Hu R, Yao Y, Xu W, Wan J. Thermally stable 2D $YMnO_3$ enabling blue visible camouflage with mid-infrared transparency. *Nat. Commun.* **2026**, *17*, 8247. DOI:10.1038/s41467-026-75174-7
11. Zhang S, Xu J, Lu C, Ouyang R, Ma J, Zhong X, et al. Preparation method investigation and structure identification by XRD and Raman techniques for $A_2B_2O_7$ composite oxides. *J. Am. Ceram. Soc.* **2024**, *107*, 3475–3496. DOI:10.1111/jace.19645
12. Matović B, Belozerova NM, Kozlenko DP, Zel IY, Maletaškić J, Zagorac D, et al. High-pressure behavior of high-entropy $A_2B_2O_7$ pyrochlore. *Ceram. Int.* **2024**, *50*, 52649–52654. DOI:10.1016/j.ceramint.2024.10.116
13. Silva RX, Paschoal CWA, Almeida RM, Castro MC, Ayala AP, Auletta JT, et al. Temperature-dependent Raman spectra of $Bi_2Sn_2O_7$ ceramics. *Vib. Spectrosc.* **2013**, *64*, 172–177. DOI:10.1016/j.vibspec.2012.05.009
14. Vijayan D, John A, Thomas JK, Solomon S. Development, characterization, and properties of $LnSmZr_2O_7$ (Ln = Dy, Ho, Yb) defect fluorite functional ceramics. *Mater. Chem. Phys.* **2023**, *307*, 128085. DOI:10.1016/j.matchemphys.2023.128085
15. Liu YX, Wang M, Shen M, Wang Q, Zhang LX. Bi-doped Ceria with Increased Oxygen Vacancy for Enhanced $CO_2$ Photoreduction Performance. *J. Inorg. Mater.* **2021**, *36*, 88. DOI:10.15541/jim20200142
16. Taniguchi T, Watanabe T, Sugiyama N, Subramani AK, Wagata H, Matsushita N, et al. Identifying Defects in Ceria-Based Nanocrystals by UV Resonance Raman Spectroscopy. *J. Phys. Chem. C* **2009**, *113*, 19789–19793. DOI:10.1021/jp9049457
17. Salke NP, Kesari S, Patwe SJ, Tyagi AK, Rao R. Raman spectroscopic studies of $Pr_2Ti_2O_7$ at high pressures. *AIP Conf. Proc.* **2015**, *1667*, 030011. DOI:10.1063/1.4917586
18. Zhong F, Duan P, Han C, Zheng Y, Cai G, Xiao Y. Pyrochlore doped $Pr_2Sn_2O_7$ ceramics: Electronic transport properties and high $NO_2$ sensitivity. *J. Eur. Ceram. Soc.* **2020**, *40*, 1376–1385. DOI:10.1016/j.jeurceramsoc.2019.11.044
19. Saha S, Muthu DVS, Singh S, Dkhil B, Suryanarayanan R, Dhalenne G, et al. Low-temperature and high-pressure Raman and x-ray studies of pyrochlore$Tb_2Ti_2O_7$: Phonon anomalies and possible phase transition. *Phys. Rev. B* **2009**, *79*, 134112. DOI:10.1103/PhysRevB.79.134112
20. Ben Li J, Kennedy BJ. Phase separation in Tb pyrochlores. Studies of $Tb_2Zr_{1-x}Sn_xO_7$. *J. Solid State Chem.* **2020**, *288*, 121386. DOI:10.1016/j.jssc.2020.121386
21. Lim S, Kim M, Ko SH, Lee JH, Baik JH, Suh YW. Efficient Cross-Coupling of Acetone with Linear Aliphatic Alcohols over Supported Copper on a Fluorite-Type $Pr_2Zr_2O_7$. *Catalysts* **2022**, *12*, 1279. DOI:10.3390/catal12101279
22. Ramon JGA, Silva PLO, Gardner JS, Freitas RS. Glassy correlated state induced by disorder in the frustrated antiferromagnet $Tb_2Zr_2O_7$. *J. Magn. Magn. Mater.* **2023**, *565*, 170215. DOI:10.1016/j.jmmm.2022.170215
23. Malathi M, Sreenu K, Ravi G, Kumar PV, Sudhakar Reddy C, Guje R, et al. Low temperature synthesis of fluorite-type Ce-based oxides of composition $Ln_2Ce_2O_7$ (Ln = Pr, Nd and Eu): Photodegradation and Luminescence studies. *J. Chem. Sci.* **2017**, *129*, 1193–1203. DOI:10.1007/s12039-017-1321-3
24. Wang C, Wang Y, Zhang A, Cheng Y, Chi F, Yu Z. The influence of ionic radii on the grain growth and sintering-resistance of $Ln_2Ce_2O_7$ (Ln = La, Nd, Sm, Gd). *J. Mater. Sci.* **2013**, *48*, 8133–8139. DOI:10.1007/s10853-013-7625-x
25. Kaur K, King G, Grosvenor AP. Examining Order–Disorder Structural Transition of $Gd_2Zr_{2-x}Ce_xO_7$ Using Synchrotron Techniques. *Inorg. Chem.* **2025**, *64*, 5913–5922. DOI:10.1021/acs.inorgchem.4c04795

26. Jalalah M, Faisal M, Bouzid H, Park JG, Al-Sayari SA, Ismail AA. Comparative study on photocatalytic performances of crystalline α- and β-$Bi_2O_3$ nanoparticles under visible light. *J. Ind. Eng. Chem.* **2015**, *30*, 183–189. DOI:10.1016/j.jiec.2015.05.020
27. Yadav P, Pandey J, Nagarajan R. Tuning the thiophilicity of $Pr_6O_{11}$ ($PrO_{1.833}$) through Pb-substitution to append efficient adsorption characteristics. *Appl. Surf. Sci.* **2022**, *591*, 153111. DOI:10.1016/j.apsusc.2022.153111
28. Chen G, Chen J, Song Z, Srinivasakannan C, Peng J. A new highly efficient method for the synthesis of rutile $TiO_2$. *J. Alloys Compd.* **2014**, *585*, 75–77. DOI:10.1016/j.jallcom.2013.09.056
29. Ristić M, Ivanda M, Popović S, Musić S. Dependence of nanocrystalline $SnO_2$ particle size on synthesis route. *J. Non-Cryst. Solids* **2002**, *303*, 270–280. DOI:10.1016/S0022-3093(02)00944-4
30. Kumari L, Du GH, Li WZ, Vennila RS, Saxena SK, Wang DZ. Synthesis, microstructure and optical characterization of zirconium oxide nanostructures. *Ceram. Int.* **2009**, *35*, 2401–2408. DOI:10.1016/j.ceramint.2009.02.007
31. Bosco MV, Bañares MA, Martínez-Huerta MV, Bonivardi AL, Collins SE. *In situ* FTIR and Raman study on the distribution and reactivity of surface vanadia species in $V_2O_5/CeO_2$ catalysts. *J. Mol. Catal. A: Chem.* **2015**, *408*, 75–84. DOI:10.1016/j.molcata.2015.07.012
32. Reddy JK, Srinivas B, Kumari VD, Subrahmanyam M. $Sm^{3+}$-Doped $Bi_2O_3$ Photocatalyst Prepared by Hydrothermal Synthesis. *ChemCatChem* **2009**, *1*, 492–496. DOI:10.1002/cctc.200900189
33. Gong YJ, He RG, Zhao GL, Jia LJ, Gao JY, Wang F, et al. Effect of Pr/Zr atomic ratio on the activity of catalytic oxidation denitration of $Pr_xZr_{1-x}O_{2-\delta}$. *J. Fuel Chem. Technol.* **2023**, *51*, 996–1005. DOI:10.1016/S1872-5813(23)60341-X
34. Li J, Zhao X, Li W, Lu P, Xia M, Zhang X, et al. Effect of $Na_2O$ on Verdet constant of Tb-doped magneto-optical glass. *Opt. Mater.* **2024**, *151*, 115388. DOI:10.1016/j.optmat.2024.115388
35. Majodina S, Mumbaraddi D, Kadaba S, Olivier J, Tshentu Z, Ogunlaja AS. Designing Ti-modified $TiO_2$-$Al_2O_3$ composites with engineered acidity, texture, and thermal stability as catalyst for hydrodesulfurization. *Mater. Today Commun.* **2026**, *51*, 114928. DOI:10.1016/j.mtcomm.2026.114928
36. Hu Y, Cao L, Gong Y, Ma X, Chen Y, Jin T. Novel $SnO_2$/ZnO gas-sensitive materials for high formaldehyde selectivity constructed by way of doping Sn into ZIF-8. *J. Alloys Compd.* **2025**, *1036*, 182018. DOI:10.1016/j.jallcom.2025.182018
37. Ma Z, Sun C, Ma C, Wu H, Zhan Z, Chen L. Ni doped $La_{0.6}Sr_{0.4}FeO_{3-\delta}$ symmetrical electrode for solid oxide fuel cells. *Chin. J. Catal.* **2016**, *37*, 1347–1353. DOI:10.1016/S1872-2067(15)61116-0
38. Liu P, Yao P, Liu X, Zeng L, Qu L, Zhang H, et al. Boosting active oxygen species formation and migration via $Bi_2O_3$ incorporation induction towards gasoline soot oxidation. *Chem. Eng. J.* **2025**, *515*, 163573. DOI:10.1016/j.cej.2025.163573
39. Zhang Y, Deng J, Zhang H, Liu Y, Dai H. Three-dimensionally ordered macroporous $Pr_6O_{11}$ and $Tb_4O_7$ with mesoporous walls: Preparation, characterization, and catalytic activity for CO oxidation. *Catal. Today* **2015**, *245*, 28–36. DOI:10.1016/j.cattod.2014.09.017
40. Wang Y, Xie Y, Zhang C, Chen W, Wang J, Zhang R, et al. Tuning the oxygen mobility of $CeO_2$ via Bi-doping for diesel soot oxidation: Experimental and DFT studies. *J. Environ. Chem. Eng.* **2021**, *9*, 105049. DOI:10.1016/j.jece.2021.105049
41. Nishino H, Yamamura H, Arai T, Kakinuma K, Nomura K. Effect of Cation Radius Ratio and Unit Cell Free Volume on Oxide-Ion Conductivity in Oxide Systems with Pyrochlore-Type Composition. *J. Ceram. Soc. Jpn.* **2004**, *112*, 541–546. DOI:10.2109/jcersj.112.541
42. Du Y, Zhu X, Wang H, Wei Y, Li K. Synthesis gas generation by chemical-looping selective oxidation of methane using $Pr_{1-x}Zr_xO_{2-\delta}$ oxygen carriers. *J. Energy Inst.* **2016**, *89*, 745–754. DOI:10.1016/j.joei.2015.04.002
43. Otsuka K, Nakajima T. Effects of additives on the reduction and oxidation of terbium oxides. *J. Catal.* **1987**, *103*, 216–219. DOI:10.1016/0021-9517(87)90110-2
44. Wu T, Wei Y, Xiong J, Yang Y, Han D, Zhao Z, et al. Atomically dispersed $SrO_x$ species on exposed {222} facets of pyrochlore $La_2Zr_2O_7$ nanocrystals for boosting low-temperature oxidative coupling of methane. *Fuel* **2023**, *333*, 126479. DOI:10.1016/j.fuel.2022.126479
45. Doornkamp C, Clement M, Ponec V. The Isotopic Exchange Reaction of Oxygen on Metal Oxides. *J. Catal* **1999**, *182*, 390–399. DOI:10.1006/jcat.1998.2377
46. Wang H, Ma C, Tian X, Cao Z, Yan L. $La_2Ce_2O_7$-based proton conductors: Defect chemistry, transport mechanisms, and application in hydrogen separation membranes. *Mater. Sci. Eng. B* **2026**, *328*, 119328. DOI:10.1016/j.mseb.2026.119328
47. Zeng J, Zhang K, Teng Y, Luo B. Influence of non-stoichiometric design concepts on the optical properties of Sm-doped $Gd_2Zr_2O_7$ transparent ceramics. *Ceram. Int.* **2025**, *51*, 16500–16508. DOI:10.1016/j.ceramint.2024.10.017
48. Quader A, Asrar A, Zawar S, Ali G, Ramay SM, Afzal F, et al. Novel La-substituted $Nd_2Ce_2O_7$ fluorite structures for efficient electrochemical performance as electrodes in supercapacitors. *Ceram. Int.* **2025**, *51*, 15123–15128. DOI:10.1016/j.ceramint.2025.01.347

49. Zhou S, Behrendt D, Rappe AM. Theoretical perspective on phase stability and polarization switching in ferroelectric hafnia. *MRS Bull.* **2025**, *50*, 1043–1052. DOI:10.1557/s43577-025-00974-z
50. Li XF, Sun YQ, Wang ZP, Mu ZG, Cui ZJ. Catalytic Combustion of Soot Particulates over Rare Earth Pyrochlore Oxides Doped with Transition Metals. *Huan Jing Ke Xue* **2017**, *38*, 1348–1356. DOI:10.13227/j.hjkx.201609228
51. Zhang D, Chen Y, Feng T, Yu D, An K, Chen R, et al. Discovery of a reversible redox-induced order-disorder transition in a 10-component compositionally complex ceramic. *Scr. Mater.* **2022**, *215*, 114699. DOI:10.1016/j.scriptamat.2022.114699